Three-Dimensional Singular Stress Fields and Interfacial Crack Path Instability in Bicrystalline Superlattices of Orthorhombic/Tetragonal Symmetries

Reaz A. Chaudhuri *

Posted Date: 22 March 2024

doi: 10.20944/preprints202403.1319.v1

Keywords: Three-dimensional; Crack; Stress Singularity; bicrystalline superlattice; Orthorhombic; Cubic, Stress Intensity Factor; Energy Release Rate

Article

Three-Dimensional Singular Stress Fields and Interfacial Crack Path Instability in Bicrystalline Superlattices of Orthorhombic/Tetragonal Symmetries

Reaz A. Chaudhuri *

Department of Materials Science & Engineering, 122 S. Central Campus Dr. Room 304, University of Utah, Salt lake City, Utah 84112-0560.

* Correspondence: r.chaudhuri@utah.edu; Tel: (801) 581-6282

Abstract. First, a recently developed eigenfunction expansion technique, based in part on separation of the thickness-variable and partly utilizing a modified Frobenius type series expansion technique in conjunction with the Eshelby-Stroh formalism, is employed to derive three-dimensional singular stress fields in the vicinity of the front of an interfacial crack weakening an infinite bicrystalline superlattice plate, made of orthorhombic (cubic, hexagonal and tetragonal serving as special cases) phases, of finite thickness and subjected to the far-field extension/bending, in-plane shear/twisting and anti-plane shear loadings, distributed through the thickness. Crack-face boundary and interface contact conditions as well as those that are prescribed on the top and bottom surfaces of the bicrystalline superlattice plate are exactly satisfied. It also extends a recently developed concept of lattice crack deflection (LCD) barrier to a superlattice, christened superlattice crack deflection (SCD) energy barrier for studying interfacial crack path instability, which can explain crack deflection from a difficult interface to an easier neighboring cleavage system. Additionally, the relationships of the nature (easy/easy, easy/difficult or difficult/difficult) interfacial cleavage systems based on the present solutions with the structural chemistry aspects of the component phases (such as orthorhombic, tetragonal, hexagonal as well as FCC (face centered cubic) transition metals and perovskites) of the superlattice are also investigated. Finally, results pertaining to the through-thickness variations of mode I/II/III stress intensity factors and energy release rates for symmetric hyperbolic sine distributed load and their skew-symmetric counterparts that also satisfy the boundary conditions on the top and bottom surfaces of the bicrystalline superlattice plate under investigation, also form an important part of the present investigation.

Keywords: three-dimensional; crack; stress singularity; bicrystalline superlattice; orthorhombic; cubic; stress intensity factor; energy release rate

1. Introduction

Leading technological developments during the last decades relate to advanced materials, which are concerned with deposition of thin films over substrates through employment of techniques, such as epitaxy, chemical vapor deposition (CVD) and physical vapor deposition (PVD) [1]. Bicrystals made of orthorhombic/cubic crystalline phases are common occurrences in many modern advanced technological applications, such as sensors [2], semiconductors [3], superconductivity [4] and so on. For example, gold nanocrystal superlattices can be formed on silicon nitride substrates with long range ordering over several microns [2]. Pashley et al. [3] have reported preparation of monocrystalline films of gold and silver onto molybdenum disulfide inside an electron microscope that permits direct observation of the mode of growth. Although considered to be non-conventional for microelectronics, grain boundary junction engineering is frequently employed in metal oxide superconductor (MOS) THz frequency applications [4]. Yin et al. [5] have employed magnetron sputtering technique to deposit superconducting $YBa_2Cu_3O_{7-d}$ (Yttrium barium copper oxide or in

 doi:10.20944/preprints202403.1319.v1

short, YBCO) thin films on four polycrystalline metal substrates, with Yttrium-stabilized zirconia (YSZ) and silver serving as buffer layers.

Asymptotic behavior of two-dimensional stress fields at the tips of cracks, anticracks (through slit cracks filled with infinitely rigid lamellas), wedges and junctions weakening/reinforcing homogeneous/bi-material/tri-material isotropic as well as anisotropic plates, has been studied extensively in the literature (see [6–15] and references therein). The mathematical difficulties posed by the three-dimensional stress singularity problems are substantially greater than their two-dimensional counterparts (to start with the governing PDE's are much more complicated). In the absence of the knowledge of the strength of singularity, in regions where the elastic stresses become unbounded, the majority of weighted residual type methods, e.g., the finite elements, finite difference and boundary elements, which are generally employed to solve fracture mechanics problems, encounter overwhelming numerical difficulties, such as lack of convergence, and oscillation resulting in poor accuracy [16]. Only an analytical solution can detail the structures of singularities related to the sharpness of a crack or anticrack, while numerical approaches can hardly have the necessary resolution [17]. The primary objective of the present investigation is to solve the crack front stress singularity problems of bicrystalline superlattice plates made of orthorhombic, tetragonal or cubic phases, subjected to mode I/II/III far-field loading, from a three-dimensional perspective.

Only recently, three-dimensional crack/anticrack/notch/antinotch/wedge front stress singularity problems have been solved by introducing a novel eigenfunction expansion technique. Various categories of three-dimensional stress singularity problems include: (i) though-thickness crack/anti-crack [18–20] as well as their bi- and tri-material interface counterparts [21–23], (ii) corresponding wedges/notches [24–28], (iii) bi-material free/fixed straight edge-face [29–31], (iv) tri-material junction [32], (v) interfacial bond line of a tapered jointed plate [33], (vi) circumferential junction corner line of an island/substrate [1], (vii) fiber-matrix interfacial debond [34–36], (viii) fiber breaks and matrix cracking in composites [37], (v) penny shaped crack/anti-crack [38,39] and their bi-material interface counterparts [40,41], (vi) through/part-through hole/rigid inclusion [42,43] and their bi-material counterparts [44,45] as well as elastic inclusion [46,47], among others. Only the penny shaped crack/anticrack [38] (and their bi-material counterparts [40]) and the hole [42] and the bi-material hole [44] and inclusion problems [46] had earlier been adequately addressed in the literature. Earlier attempts to solve the three-dimensional through crack problem resulted in controversies that lasted for about a quarter century [18,19]. A unified three-dimensional eigenfunction approach has recently been developed by Chaudhuri and co-workers [1,18–38,41,43,45,47] to address the three-dimensional stress singularity problems covering all the aspects mentioned above. These facts not only lend credence to the validity of the afore-mentioned three-dimensional eigenfunction expansion approach, but also reinforce the afore-mentioned conceptual as well as mathematical similarity of and linkages among the afore-cited classes of three-dimensional stress singularity problems.

The above separation of variables approach has recently been extended to cubic and orthorhombic/orthotropic and monoclinic/anisotropic materials [48–55]. Cracked/anticracked transversely isotropic (smeared-out composite) [48] as well as cubic/orthorhombic/diamond cubic mono-crystalline plates subjected to mode I/II far-field loadings [49–51] and cubic/orthorhombic/monoclinic/diamond cubic mono/tri-crystalline plates under mode III loading [49,51–54] have been solved by a novel three-dimensional eigenfunction expansion technique, based in part on the above-mentioned separation of the thickness-variable and partly an affine transformation, that is similar (but not identical) in spirit to that due to Eshelby et al. [56] and Stroh [7]. This eigenfunction expansion approach has also recently been employed to obtain three-dimensional asymptotic stress fields in the vicinity of the front of the kinked carbon fiber-matrix junction [55] (see also Ref. [14] for its 2D counterpart with isotropic glass fibers).

In what follows, the afore-mentioned modified eigenfunction expansion technique [48–55], based in part on separation of the thickness-variable and partly utilizing a modified Frobenius type series expansion technique in conjunction with the Eshelby-Stroh formalism, is employed to derive heretofore unavailable three-dimensional singular stress fields in the vicinity of the front of an interfacial crack weakening an infinite bicrystalline superlattice plate, made of orthorhombic (cubic,

 doi:10.20944/preprints202403.1319.v1

hexagonal and tetragonal serving as special cases) phases, of finite thickness and subjected to the far-field extension/bending, in-plane shear/twisting and anti-plane shear loadings, distributed through the thickness. Crack-face boundary and interface contact conditions as well as those that are prescribed on the top and bottom surfaces of the bicrystalline superlattice plate are exactly satisfied. This has applications in electronic packaging industry, fiber reinforced composites [55], earthquake physics, mining, among many others.

The second and more important objective is to extend a recently developed concept of lattice crack deflection (LCD) barrier [49,59] to a superlattice, christened superlattice crack deflection (SCD) energy barrier for studying interfacial crack path instability, which can explain crack deflection from a difficult interface to an easier neighboring cleavage system. Additionally, the relationships of the nature (easy/easy, easy/difficult or difficult/difficult) interfacial cleavage systems based on the present solutions with the structural chemistry aspects of the component phases (such as orthorhombic, tetragonal, hexagonal as well as FCC (face centered cubic) transition metals and perovskites) of the superlattice are also investigated. Finally, results pertaining to the through-thickness variations of mode I/II/III stress intensity factors and energy release rates for symmetric hyperbolic sine distributed load and their skew-symmetric counterparts that also satisfy the boundary conditions on the top and bottom surfaces of the bicrystalline superlattice plate under investigation, also form an important part of the present investigation.

2. Statement of the Problem

The Cartesian coordinate system (x, y, z) is convenient to describe the deformation behavior in the vicinity of the front of an interfacial semi-infinite crack weakening an infinite pie-shaped bicrystalline superlattice plate. The thickness of the bicrystalline superlattice plate is 2h (Figure 1). The cylindrical polar coordinate system, (r, q, z), is, however, more convenient to describe the boundary and interfacial contact conditions. The x-y plane serves as the interfacial plane. Here, the z-axis ($|z| \leq h$) is placed along the straight crack front, while the coordinates r, q or x, y are used to define the position of a point in the plane of the plate (see Figure 1). The bicrystalline superlattice interface between materials 1 and 2 is located at $q = 0$, i.e., it coincides with the positive x-axis, while the crack-side faces are located at $q = \pm p$ (Figure 1). Components of the displacement vector in the j^{th} crystal ($j = 1, 2$) in x and y directions are demoted by u_j and v_j, while the component in the z-direction is denoted by w_j, $j = 1, 2$. The displacement components in the radial and tangential directions are represented by u_{rj} and u_{qj}, respectively.

Preprints.org (www.preprints.org) | NOT PEER-REVIEWED | Posted: 22 March 2024 doi:10.20944/preprints202403.1319.v1

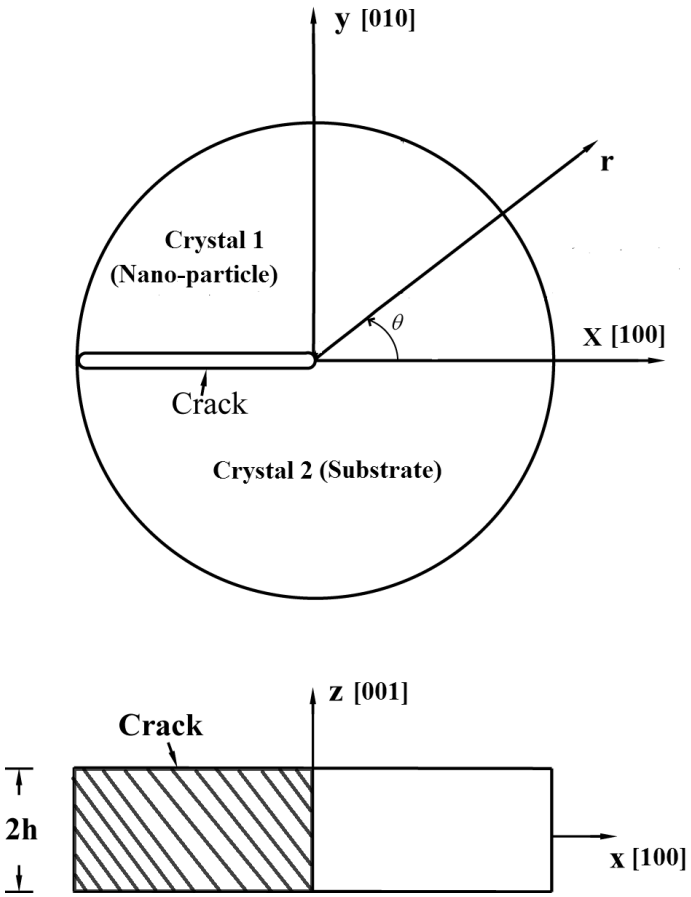

Figure 1. Schematic of a bicrystalline superlattice plate with an interfacial crack.

In what follows, σ_{xj}, σ_{yj} and σ_{zj} represent the normal stresses, while τ_{yzj}, τ_{xzj} and τ_{xyj} denote the shear stresses. ε_{xj}, ε_{yj} and ε_{zj} are the normal strains, while γ_{yzj}, γ_{xzj} and γ_{xyj} represent shear strains. $c_{i\ell}^{(j)}$, i, l = 1,...,6, denotes the elastic stiffness constants of j[th] orthorhombic material, given in the form:

$$\begin{Bmatrix} \sigma_{xj} \\ \sigma_{yj} \\ \sigma_{zj} \\ \tau_{yzj} \\ \tau_{xzj} \\ \tau_{xyj} \end{Bmatrix} = \begin{bmatrix} c_{11}^{(j)} & c_{12}^{(j)} & c_{13}^{(j)} & 0 & 0 & 0 \\ c_{12}^{(j)} & c_{22}^{(j)} & c_{23}^{(j)} & 0 & 0 & 0 \\ c_{13}^{(j)} & c_{23}^{(j)} & c_{33}^{(j)} & 0 & 0 & 0 \\ 0 & 0 & 0 & c_{44}^{(j)} & 0 & 0 \\ 0 & 0 & 0 & 0 & c_{55}^{(j)} & 0 \\ 0 & 0 & 0 & 0 & 0 & c_{66}^{(j)} \end{bmatrix} \begin{Bmatrix} \varepsilon_{xj} \\ \varepsilon_{yj} \\ \varepsilon_{zj} \\ \gamma_{yzj} \\ \gamma_{xzj} \\ \gamma_{xyj} \end{Bmatrix}. \quad (1)$$

In the absence of body forces, the coupled partial differential equations for a linear elastic crystalline solid in terms of the displacement functions u_j, v_j and w_j, are given as follows:

$$c_{11}^{(j)}\frac{\partial^2 u_j}{\partial x^2}+c_{66}^{(j)}\frac{\partial^2 u_j}{\partial y^2}+c_{55}^{(j)}\frac{\partial^2 u_j}{\partial z^2}+(c_{12}^{(j)}+c_{66}^{(j)})\frac{\partial^2 v_j}{\partial x\partial y}+(c_{13}^{(j)}+c_{55}^{(j)})\frac{\partial^2 w_j}{\partial x\partial z}=0, \quad (2a)$$

$$(c_{12}^{(j)}+c_{66}^{(j)})\frac{\partial^2 u_j}{\partial x\partial y}+c_{66}^{(j)}\frac{\partial^2 v_j}{\partial x^2}+c_{22}^{(j)}\frac{\partial^2 v_j}{\partial y^2}+c_{44}^{(j)}\frac{\partial^2 v_j}{\partial z^2}+(c_{23}^{(j)}+c_{44}^{(j)})\frac{\partial^2 w_j}{\partial y\partial z}=0, \quad (2b)$$

$$(c_{13}^{(j)}+c_{55}^{(j)})\frac{\partial^2 u_j}{\partial x\partial z}+(c_{23}^{(j)}+c_{44}^{(j)})\frac{\partial^2 v_j}{\partial y\partial z}+c_{55}^{(j)}\frac{\partial^2 w_j}{\partial x^2}+c_{44}^{(j)}\frac{\partial^2 w_j}{\partial y^2}$$

 doi:10.20944/preprints202403.1319.v1

$$+c_{33}^{(j)}\frac{\partial^2 w_j}{\partial z^2}=0, \qquad j=1,2 \tag{2c}$$

The boundary conditions on the bicrystalline superlattice plate surfaces, z = ±h, are given as follows:

Traction-free (see Section 6 below):

$$\sigma_{zj} = \tau_{xzj} = \tau_{yzj} = 0, \qquad j=1,2. \tag{3}$$

The interfacial contact conditions as well as boundary conditions at the crack-side surfaces (valid for r > 0) are more conveniently expressed in local cylindrical polar coordinates (Figure 1). Assuming that the bicrystalline superlattice interface at q = 0 is always perfectly bonded, it is easy to establish the continuity conditions of the stresses and displacements along this interface as follows:

$$\text{(i) } q=0: \quad u_{\theta 1}=u_{\theta 2},\ u_{r1}=u_{r2},\ u_{z1}=u_{z2}, \tag{4a}$$

$$\sigma_{\theta 1}=\sigma_{\theta 2},\ \tau_{r\theta 1}=\tau_{r\theta 2},\ \tau_{\theta z1}=\tau_{\theta z2}. \tag{4b}$$

The boundary conditions at the crack-side surfaces, at q = ±π, are as given below:

$$\sigma_{\theta 1}(\pi)= \tau_{r\theta 1}(\pi) = \tau_{\theta z1}(\pi) = 0, \tag{5a}$$

$$\sigma_{\theta 2}(-\pi)= \tau_{r\theta 2}(-\pi) = \tau_{\theta z2}(-\pi) = 0, \tag{5b}$$

where s_{rj}, s_{qj} and s_{zj} represent the normal stresses, and t_{rqj}, t_{rzj} and t_{qzj} denote the shear stresses in the j^{th} crystal (j = 1, 2) in the cylindrical polar coordinate system (r, q, z).

3. Singular Stress Fields in the Vicinity of a Crack Front Weakening a Bicrystalline Superlattice with Orthorhombic Phases under General Loading

The assumed displacement functions for the j^{th} crystal (j = 1, 2) for the three-dimensional interfacial crack problem under consideration are selected on the basis of separation of z-variables. These are as given below [48–55]:

$$u_j(x,y,z) = e^{i\alpha z}U_j(x,y),\quad v_j(x,y,z) = e^{i\alpha z}V_j(x,y),\quad w_j(x,y,z) = e^{i\alpha z}W_j(x,y), \tag{6a,b,c}$$

where a is a constant, called the wave number, required for a Fourier series expansion in the z-direction. It may be noted that since the separated z-dependent term and its first partial derivative can either be bounded and integrable at most admitting ordinary discontinuities, or the first partial derivative at worst be square integrable (in the sense of Lebesgue integration) in its interval z ∈ [-h, h], i.e., admitting singularities weaker than square root (i.e., $z^{(-1/2+e)}$, e > 0 being a very small number), it can be best represented by Fourier series [48–55]. The latter case is justified by the Parseval theorem [57], and its physical implication is that of satisfying the criterion of finiteness of local strain energy and path independence [58]. Substitution of Eqs. (6) into Eqs. (2) yields the following system of coupled partial differential equations (PDE's):

$$c_{11}^{(j)}\frac{\partial^2 U_j}{\partial x_1^2}+c_{66}^{(j)}\frac{\partial^2 U_j}{\partial y_1^2}+c_{55}^{(j)}U_j+(c_{12}^{(j)}+c_{66}^{(j)})\frac{\partial^2 V_j}{\partial x_1\partial y_1}+(c_{13}^{(j)}+c_{55}^{(j)})\frac{\partial W_j}{\partial x_1}=0, \tag{7a}$$

$$(c_{12}^{(j)}+c_{66}^{(j)})\frac{\partial^2 U_j}{\partial x_1\partial y_1}+c_{66}^{(j)}\frac{\partial^2 V_j}{\partial x_1^2}+c_{22}^{(j)}\frac{\partial^2 V_j}{\partial y_1^2}+c_{44}^{(j)}V_j+(c_{23}^{(j)}+c_{44}^{(j)})\frac{\partial W_j}{\partial y_1}=0, \tag{7b}$$

$$(c_{13}^{(j)}+c_{55}^{(j)})\frac{\partial U_j}{\partial x_1}+(c_{23}^{(j)}+c_{44}^{(j)})\frac{\partial V_j}{\partial y_1}+c_{55}^{(j)}\frac{\partial^2 W_j}{\partial x_1^2}+c_{44}^{(j)}\frac{\partial^2 W_j}{\partial y_1^2}+c_{33}^{(j)}W_j=0, \tag{7c}$$

where

$$x_1 = i\alpha x, \qquad y_1 = i\alpha y. \tag{8a,b}$$

The solution to the system of coupled partial differential equations (7) subjected to the most general loading, can now be sought in the form of the following modified Frobenius type series in terms of the variable x_1+py_1 as follows:

 doi:10.20944/preprints202403.1319.v1

$$U(x_1,y_1) = \sum_{n=0}^{\infty} a'_{s+n}\ (x_1+py_1)^{s+2n+1} + \sum_{n=0}^{\infty} \bar{a}_{s+n}\ (x_1+py_1)^{s+2n}, \tag{9a}$$

$$V(x_1,y_1) = \sum_{n=0}^{\infty} b'_{s+n}\ (x_1+py_1)^{s+2n+1} + \sum_{n=0}^{\infty} \bar{b}_{s+n}\ (x_1+py_1)^{s+2n}, \tag{9b}$$

$$W(x_1,y_1) = \sum_{n=0}^{\infty} c'_{s+n}\ (x_1+py_1)^{s+2n} + \sum_{n=0}^{\infty} \bar{c}_{s+n}\ (x_1+py_1)^{s+2n+1}. \tag{9c}$$

For an orthorhombic lamina, out of the various combinations given above, such as (a'_{sn}, b'_{sn}, c'_{sn}), ($\bar{a}_{sn}$, $\bar{b}_{sn}$, $\bar{c}_{sn}$), (a'_{sn}, $\bar{b}_{sn}$, $\bar{c}_{sn}$), ($\bar{a}_{sn}$, b'_{sn}, $\bar{c}_{sn}$), ($\bar{a}_{sn}$, $\bar{b}_{sn}$, c'_{sn}), (a'_{sn}, b'_{sn}, $\bar{c}_{sn}$), (a'_{sn}, $\bar{b}_{sn}$, c'_{sn}), and ($\bar{a}_{sn}$, b'_{sn}, c'_{sn}), only the first two groupings can produce meaningful solutions, for the mode III and mode I/II loading cases, respectively. This step permits separation of the mode III from the modes I/II for the problem under investigation. The first grouping is described below, while the second one has earlier been employed for the anti-plane shear case [49,51–54].

4. Singular Stress Fields in the Vicinity of a (010)[001] Through-Thickness Crack Front Propagating under Mode I (Extension/Bending) and Mode II (Sliding Shear/Twisting) in [100] Direction

The solution to the system of coupled partial differential equations (7), subjected to the far-field mode I (extension/bending) and mode II (sliding shear/twisting) loading, can now be sought in the form of the following modified Frobenius type series in terms of the variable x_1+py_1 as follows [48–51], although unlike in the case of isotropic materials [18–26,29–33], the x_1 and y_1 variables are no longer separable:

$$U_j(x_1,y_1) = \sum_{n=0}^{\infty} \bar{a}_{sj+n}\ (x_1+p^{(j)}y_1)^{s+2n}, \tag{10a}$$

$$V_j(x_1,y_1) = \sum_{n=0}^{\infty} \bar{b}_{sj+n}\ (x_1+p^{(j)}y_1)^{s+2n}, \tag{10b}$$

$$W_j(x_1,y_1) = \sum_{n=0}^{\infty} \bar{c}_{sj+n}\ (x_1+p^{(j)}y_1)^{s+2n+1}. \tag{10c}$$

Here, s represents a fractional exponent, while n denotes an integer in the power series. The combined variable x_1+py_1 represents an affine transformation in the same spirit as that by Eshelby et al. [56] and Stroh [7], although these latter authors have employed completely different techniques. Substitution of Eqs. (10) into Eqs. (7), and equating the coefficients of $(x_1+p^{(j)}y_1)^{s+2n-2}$ yields the following two recurrent relations:

$$(s+2n)(s+2n-1)\ (c_{11}+c_{66}p^{(j)^2})\ \bar{a}_{s+n} + c_{55}\ \bar{a}_{s+n-1} + (s+2n)(s+2n-1)\ (c_{12}+c_{66})p^{(j)}\ \bar{b}_{s+n} + (s+2n-1)\ (c_{13}+c_{55})\ \bar{c}_{s+n-1} = 0, \tag{11a}$$

$$(s+2n)(s+2n-1)\ (c_{12}+c_{66})p^{(j)}\ \bar{a}_{s+n} + (s+2n)(s+2n-1)\ (c_{22}+c_{66}p^{(j)^2})\ \bar{b}_{s+n} + c_{44}\ \bar{b}_{s+n-1} + (s+2n-1)\ (c_{23}+c_{44})\ \bar{c}_{s+n-1} = 0, \tag{11b}$$

which for n = 0, reduces to

$$\begin{bmatrix} c_{11}+c_{66}p^{(j)^2} & (c_{12}+c_{66})p^{(j)} \\ (c_{12}+c_{66})p^{(j)} & c_{22}p^{(j)^2}+c_{66} \end{bmatrix} \begin{Bmatrix} \bar{a}_s \\ \bar{b}_s \end{Bmatrix} = \begin{Bmatrix} 0 \\ 0 \end{Bmatrix}, \quad \text{for } s \neq 0, 1. \tag{12}$$

The characteristic equation for the coupled partial differential equations (2) or (7) can now be written as follows:

 doi:10.20944/preprints202403.1319.v1

$$p^{(j)4} + 2\chi^{(j)} p^{(j)2} + \frac{c_{11}^{(j)}}{c_{22}^{(j)}} = 0,\ j = 1,2 \tag{13}$$

where the normalized elastic parameter, $\kappa^{(j)} = 1/\chi^{(j)}$, is given b

$$\kappa^{(j)} = \frac{1}{\chi^{(j)}} = \frac{2c_{22}^{(j)}c_{66}^{(j)}}{(c_{11}^{(j)}c_{22}^{(j)} - c_{12}^{(j)2} - 2c_{12}^{(j)}c_{66}^{(j)})},\ j = 1,2 \quad . \tag{14a}$$

It also is sometimes convenient to relate $\kappa = 1/\chi$, as will be seen later, to $A = 1/\lambda$, with $\tilde{A}$ being the planar anisotropic ratio (in the x [100]-y [010] plane), as shown below $\kappa^{(j)}$, j = 1, 2, can also be expressed in terms of the planar anisotropic ratio (in the x-y plane), $A^{(j)}$, as follows:

$$\kappa^{(j)} = \frac{A^{(j)}c_{22}^{(j)}}{\sqrt{c_{11}^{(j)}c_{22}^{(j)}} + c_{12}^{(j)}\left(1 - A^{(j)}\right)},\ j = 1,2, \tag{14b}$$

where

$$A^{(j)} = \frac{2c_{66}^{(j)}}{\sqrt{c_{11}^{(j)}c_{22}^{(j)}} - c_{12}^{(j)}},\ j = 1,2, \tag{15}$$

It can easily be seen from Eq. (15) that A is higher when the shear stiffness (modulus) and major Poisson's ratio in the x [100], y [010] plane assume larger magnitudes. This simple fact assumes great importance as this investigation aims to solve one Holy Grail issue, in fracture mechanics of anisotropic media, of coming up with a dimensionless parameter akin to Reynold's number in fluid flow problems, crossing a critical value of which signifies transition from one regime to another, such as the critical value of Reynold's number above which the flow is turbulent and below which it is laminar. It is an attendant issue relating to crack deflection in mono-crystalline orthorhombic laminas [59].

Eq. (13) has either (a) four complex or (b) four imaginary roots, depending on whether:

(a) $A^{(j)} > 1$ or equivalently, $\left|\kappa^{(j)}\right| > \sqrt{\frac{c_{11}^{(j)}}{c_{22}^{(j)}}}$, (16a)

or (b) $A^{(j)} < 1$ or equivalently, $\left|\kappa^{(j)}\right| < \sqrt{\frac{c_{11}^{(j)}}{c_{22}^{(j)}}}$, (16b)

$A^{(j)} = 1$ or $\kappa^{(j)} = 1$ represents the degenerate isotropic material case, for which the solution is available in Chaudhuri and Xie [18,19].

Case (a): Complex Roots

$$p_{1,2} = \xi^{(j)} \pm i\eta^{(j)}, \qquad p_{3,4} = -\xi^{(j)} \pm i\eta^{(j)}, \tag{17a, b}$$

where

$$\xi^{(j)} = \frac{1}{\sqrt{2}}\left[\left(\frac{c_{11}^{(j)}}{c_{22}^{(j)}}\right)^{1/2} - \frac{1}{\kappa^{(j)}}\right]^{1/2}, \quad \eta^{(j)} = \frac{1}{\sqrt{2}}\left[\left(\frac{c_{11}^{(j)}}{c_{22}^{(j)}}\right)^{1/2} + \frac{1}{\kappa^{(j)}}\right]^{1/2}, \tag{18a.b}$$

valid for $\left|\kappa^{(j)}\right| > \sqrt{\frac{c_{11}^{(j)}}{c_{22}^{(j)}}}$.

Case (b): Imaginary Roots

The four imaginary roots of Eq. (13) are given by

$$p_{1,2} = \pm i\left(\xi'^{(j)} + i\eta'^{(j)}\right),\ p_{3,4} = \pm i\left(\xi'^{(j)} - i\eta'^{(j)}\right), \tag{19a,b}$$

where

 doi:10.20944/preprints202403.1319.v1

$$\xi'^{(j)} = \frac{1}{\sqrt{2}}\left[\left(\frac{c_{11}^{(j)}}{c_{22}^{(j)}}\right)^{1/2} + \frac{1}{\kappa'^{(j)}}\right]^{1/2}, \quad \xi''^{(j)} = \frac{1}{\sqrt{2}}\left[-\left(\frac{c_{11}^{(j)}}{c_{22}^{(j)}}\right)^{1/2} + \frac{1}{\kappa'^{(j)}}\right]^{1/2}, \tag{20a,b}$$

valid for $\left|\kappa'^{(j)}\right| < \sqrt{\frac{c_{11}^{(j)}}{c_{22}^{(j)}}}$,

5. Satisfaction of Crack Face Boundary and Interfacial Contact Conditions

5.1. Both Crystal Layers with Complex Roots

For the case of both crystal layers with complex roots, substitution of Eqs. (A6a,b) as well as Eqs. (A2b,c) in conjunction with Eqs. (A7), into the left and right hand sides of Eqs. (4a,b) would yield four homogeneous equations. In addition, substitution of Eqs. (A2b,c) in conjunction with Eqs. (A7), into the left hand sides of Eqs. (5a,b) would yield another set of four homogeneous equations. These can be expressed in the compact form as follows:

$$\left[\Delta(s)\right]\left\{A_{ij}\right\} = 0. \tag{21a}$$

The existence of a nontrivial solution for A_{ij} requires vanishing of the coefficient determinant

$$\left|\Delta(s)\right| = 0. \tag{21b}$$

$\Delta(s)$ is an 8×8 matrix involving s in a transcendental form. The solution that has physical meaning is given by 0< Re(s) < 1. Here $s = 0.5 \pm i\varepsilon$, in which e is obtained from the following relationships, obtained by equating the real and imaginary parts:

Real Part:

$$a\cosh^4(\varepsilon\pi) - b\cosh^2(\varepsilon\pi) + c = 0, \tag{22}$$

Eq. (22) yields

$$\cosh(\varepsilon\pi) = \left\{\frac{-b \pm \sqrt{b^2 - 4ac}}{2a}\right\}^{1/2}, \tag{23}$$

where

$$a = -(a_1e_1 + b_1f_1)c_2{}^2d_1f_1, \tag{24a}$$

$$b = c_2f_1\left\{a_1c_2(a_1c_1 + b_1d_1) - (c_1f_1 - d_1e_1)(b_2(d_1 + d_2) + a_2c_2)\right\}, \tag{24b}$$

$$c = a_1b_2c_2d_1(c_1f_1 - d_1e_1). \tag{24c}$$

where

$$a_1 = c_{12}^{(1)} + c_{22}^{(1)}\left(H_{11}\xi^{(1)} - H_{21}\eta^{(1)}\right), \quad b_1 = c_{22}^{(1)}\left(H_{11}\xi^{(1)} + H_{21}\eta^{(1)}\right), \tag{25a,b}$$

$$c_1 = H_{11} + \xi^{(1)}, \quad d_1 = H_{21} + \eta^{(1)}, \tag{25c,d}$$

$$a_2 = c_{12}^{(2)} + c_{22}^{(2)}\left(H_{12}\xi^{(2)} - H_{22}\eta^{(2)}\right), \quad b_2 = c_{22}^{(2)}\left(H_{22}\xi^{(2)} + H_{12}\eta^{(2)}\right), \tag{26a,b}$$

$$c_2 = H_{12} + \xi^{(2)}, \quad d_2 = H_{22} + \eta^{(2)}, \tag{26c,d}$$

$$e_1 = \frac{H_{11}(a_2c_2 + b_2d_2) - c_1(H_{12}a_2 - H_{22}b_2)}{H_{22}c_2 + H_{12}d_2}, \tag{27a}$$

$$f_1 = \frac{H_{21}(a_2c_2 + b_2d_2) - d_1(H_{12}a_2 - H_{22}b_2)}{H_{22}c_2 + H_{12}d_2}. \tag{27b}$$

Imaginary Part:

$$a''\cosh^4(\varepsilon''\pi) + b''\cosh^2(\varepsilon''\pi) + c'' = 0, \tag{28}$$

where

$$a'' = c + d - e, \ b'' = e - 2c''. \tag{29}$$

 doi:10.20944/preprints202403.1319.v1

Eq. (27) yields

$$\cosh\left(\delta''\pi\right)=\left\{\frac{-\left(e-2c''\right)\pm\sqrt{e^2-4dc''}}{2\left(d-e+c''\right)}\right\}^{1/2}, \tag{30}$$

in which

$$c''=a_1b_2^2d_1\left(c_1f_1-d_1e_1\right), \tag{31a}$$

$$d=c_2f_1\left(a_1e_1+b_1f_1\right)\left\{b_2d_2-c_2\left(a_1-a_2\right)\right\}, \tag{31b}$$

$$e=a_1b_2c_2d_1\left(a_1e_1+b_1f_1\right)+\left(c_1f_1-d_1e_1\right)\left(a_2b_2c_2f_1-b_2^2d_2f_1-a_1^2b_2c_2\right), \tag{31c}$$

5.2. Both Crystal Layers with Imaginary Roots

Similarly, for the case of both crystal layers with imaginary roots, substitution of Eqs. (B5a,b) as well as Eqs. (B2b,c) in conjunction with Eqs. (A7), into the left and right hand sides of Eqs. (4a,b) would also yield four homogeneous equations. Additionally, substitution of Eqs. (B2b,c), into the left hand sides of (5a,b) would yield another set of four homogeneous equations. Proceeding in a similar manner, one obtains $s=0.5\pm i\varepsilon'\pi$, in which ε' is obtained from the relationship:

$$a'\cosh^4\left(\varepsilon'\pi\right)+b'\cosh^2\left(\varepsilon'\pi\right)+c'=0. \tag{32}$$

Eq. (32) yields

$$\cosh\left(\varepsilon'\pi\right)=\left\{\frac{-b'\pm\sqrt{b'^2-4a'c'}}{2a'}\right\}^{1/2}, \tag{33}$$

where

$$a'=f_1'f_2'\left(-2a_1'b_1'c_1'd_1'+a_1'^2d_1'^2+e_1'^2\right)+2a_1'^2d_1'e_1'e_2'f_1'+a_1'c_1'e_2'\left(a_2'-b_2'\right)\left(e_1'^2+b_1'^2c_1'^2+a_1'^2d_1'^2\right), \tag{34a}$$

$$b'=f_1'f_2'\left(2a_1'b_1'c_1'd_1'-a_1'^2d_1'^2-e_1'^2\right)+a_1'e_1'e_2'f_1'\left(b_1'c_1'-2a_1'd_1'\right)+a_1'c_1'\left(a_1'd_1'-b_1'c_1'\right)\left(f_1g_2-f_2g_1\right)$$
$$+a_1'c_1'\left(a_2'-b_2'\right)\left(c_1'e_1'g_2'-d_1'e_1'f_2'+b_1'^2c_1'^2e_2'-2e_1'^2e_2'-a_1'^2d_1'^2e_2'\right), \tag{34b}$$

$$c'=-a_1'b_1'c_1'd_1'f_1'f_2'+a_1'c_1'e_1'e_2'\left(a_1'g_1'-b_1'f_1'\right)+a_1'c_1'\left(a_1'd_1'+b_1'c_1'\right)\left(f_1'g_2'+f_2'g_1'\right)$$
$$-a_1'^2c_1'^2g_1'g_2'+a_1'c_1'e_1'\left(a_2'-b_2'\right)\left(e_1'e_2'-c_1'g_2'+d_1'f_2'\right), \tag{34c}$$

in which

$$a_1'=c_{12}^{(1)}+c_{22}^{(1)}H_{11}'\left(\xi_1'^{(1)}+\eta_1'^{(1)}\right),\quad b_1'=c_{12}^{(1)}+c_{22}^{(1)}H_{21}'\left(\xi_1'^{(1)}-\eta_1'^{(1)}\right), \tag{35a,b}$$

$$c_1'=H_{11}'-\left(\xi_1'^{(1)}+\eta_1'^{(1)}\right),\quad d_1'=H_{21}'-\left(\xi_1'^{(1)}-\eta_1'^{(1)}\right), \tag{35c,d}$$

$$a_2'=c_{12}^{(2)}+c_{22}^{(2)}H_{12}'\left(\xi_1'^{(2)}+\eta_1'^{(2)}\right),\quad b_2'=c_{12}^{(2)}+c_{22}^{(2)}H_{22}'\left(\xi_1'^{(2)}-\eta_1'^{(2)}\right), \tag{36a,b}$$

$$c_2'=H_{12}'-\left(\xi_1'^{(2)}+\eta_1'^{(2)}\right),\quad d_2'=H_{22}'-\left(\xi_1'^{(2)}-\eta_1'^{(2)}\right), \tag{36c,d}$$

$$e_1'=b_1'c_1'-a_1'd_1',\quad f_1'=c_2'\left(a_1'-b_2'\right)-d_2'\left(a_1'-a_2'\right),\quad g_1'=c_2'\left(b_1'-b_2'\right)-d_2'\left(b_1'-a_2'\right), \tag{37a,b,c}$$

$$e_2'=H_{22}'c_1'-H_{12}'d_1',\quad f_2'=b_2'\left(H_{12}'c_1'-H_{11}'c_2'\right)-\left(H_{22}'a_1'c_1'+H_{11}'a_2'd_2'\right), \tag{38a,b}$$

$$g_2'=H_{21}'\left(b_2'c_2'-a_2'd_2'\right)+d_1'\left(H_{22}'a_2'-H_{12}'b_2'\right). \tag{38c}$$

5.3. Top Crystal (Layer 1) with Complex Roots and Bottom Crystal (Layer 2) with Imaginary Roots

For the case of top crystal (layer 1) with complex roots and bottom crystal (layer 2) with imaginary roots, substitution of Eqs. (A6a,b) as well as Eqs. (A2b,c) in conjunction with Eqs. (A7),

 doi:10.20944/preprints202403.1319.v1

into the left, and that of Eqs. (B5a,b) as well as Eqs. (B2b,c), in conjunction with Eqs. (A7) into the right hand sides of Eqs. (4a,b) would yield four homogeneous equations.

In addition, substitution of Eqs. (A2b,c) in conjunction with Eqs. (A7), into the left hand sides of Eqs. (5a) would yield another set of two homogeneous equations. Likewise, substitution of Eqs. (B2b,c), into the left hand sides of (5b) would yield the remaining set of two homogeneous equations. Proceeding in a similar manner as above, one obtains $s = 0.5 \pm i\bar{\varepsilon}\pi$, in which $\bar{\varepsilon}$ is obtained from the relationship:

$$\bar{a}\cosh^4\left(\bar{\varepsilon}\pi\right) + \bar{b}\cosh^2\left(\bar{\varepsilon}\pi\right) + \bar{c} = 0, \tag{39}$$

Eq. (36) yields

$$\cosh\left(\bar{\varepsilon}\pi\right) = \left\{\frac{-\bar{b} \pm \sqrt{\bar{b}^2 - 4\bar{a}\bar{c}}}{2\bar{a}}\right\}^{1/2}, \tag{40}$$

where

$$\bar{a} = \bar{d} - \bar{e}\bar{g},\ \bar{b} = \bar{d} - \bar{e}\bar{h} - \bar{f}\bar{g},\ \bar{c} = -\bar{f}\bar{h}, \tag{41}$$

in which

$$\bar{d} = \bar{e}_1^2\left(H_{11}\bar{f}_1 + c_1\bar{e}_2 + b_1\bar{f}_2\right)\left[a_1\left(c_2 - d_2\right) - d_1\left(a_2 - b_2\right) - \bar{f}_1\right], \tag{42a}$$

$$\bar{e} = -\bar{e}_1\left(H_{21}\bar{f}_1 + d_1\bar{e}_2 - a_1\bar{f}_2\right), \qquad \bar{f} = -d_1\bar{e}_1\left(\bar{f}_1 + \bar{e}_2\right), \tag{42b,c}$$

$$\bar{g} = b_1\bar{e}_1\left(c_2 - d_2\right), \qquad \bar{h} = b_1\left[c_1\bar{f}_1 + \bar{e}_1\left(c_2 - d_2\right)\right], \tag{42d,e}$$

where

$$\bar{e}_1 = a_1c_1 + b_1d_1, \quad \bar{f}_1 = b_2c_2 - a_2d_2, \quad \bar{e}_2 = a_2H'_{22} - b_2H'_{12}, \quad \bar{f}_2 = c_2H'_{22} - d_2H'_{12}. \tag{43a,b,c,d}$$

It may be noted that for a homogeneous solution such as what is presented above, the seven eigenvector components, $A_{12}(z)$, $A_{21}(z),\ldots, A_{42}(z)$ cannot be evaluated in absolute terms, but can only be expressed in terms of the eighth component, $A_{11}(z)$, which can be related to the "stress intensity factors", $K_{Ij}(z)$ and $K_{IIj}(z)$, which can, in turn, be resolved as follows:

$$K_{Ij}(z) = K_{Ijs}(z) + K_{Ija}(z), \qquad K_{IIj}(z) = K_{IIjs}(z) + K_{IIja}(z), \tag{22a,b}$$

in which $K_{Ijs}(z)$ and $K_{IIjs}(z)$, j = 1, 2, represent the symmetric (with respect to z) mode I and mode II stress intensity factors, which correspond to in-plane extension and sliding shear, respectively. $K_{Ija}(z)$ and $K_{IIja}(z)$, j = 1, 2, denote the antisymmetric (with respect to z) mode I and mode II stress intensity factors, which correspond to bending and twisting, respectively.

The stress intensity factors, and the energy release rates are found to be as follows:

$$K_{I/IIj}\left(z\right) = K_{I/IIj,2D}D_{bj}\left(z\right), G_{I/IIj}\left(z\right) = G_{I/IIj,2D}\left[D_{bj}\left(z\right)^2\right], \tag{23a,b}$$

in which $K_{I/IIj,2D}$ and $G_{I/IIj,2D}$ are available in the published literature; see e.g., Wu [10] and Wang et al. [13]. In what follows, the primary focus will be on three-dimensionality and lattice (more specifically super-lattice) fracture aspects of bi-crystals.

6. Boundary Conditions on the Bicrystalline Superlattice Plate Surfaces and Through-Thickness Distribution of Singular Stress Fields

6.1. General Distributed Far-Field Loading

By using the traction-free boundary conditions at the top and bottom surfaces, z* = z/h = ±1, of the plate, given by Eqs. (3), the general form of $D_{bj}(z)$, defined in Eq. (A3), can be obtained. The stress field that satisfies traction-free boundary conditions at z* = ± 1, in the vicinity of the front of a bi-material interface crack under extension/sliding shear, can be recovered if in Eqs. (A3):

 doi:10.20944/preprints202403.1319.v1

$$D_{bj}(z) = D_{bs\,j}(z) = D_{2\,j}\cos(\alpha z), \qquad j = 1,2 \tag{23}$$

By substituting Eq. (A2d) or Eq. (B2d) into the boundary condition on the singular-stress-free surface of a cracked bicrystalline superlattice plate, given by Eq. (3), the general form of $D_{bs\,j}(z)$ can be obtained as follows:

$$D_{bsj}(z) = \sum_{m=0}^{\pm\infty} D_{1mj}\cos\left(\frac{(2m+1)\pi z^*}{2}\right), \qquad j = 1,2. \tag{24}$$

Hence, $K_I = K_{Is}$ and $K_{II} = K_{IIs}$ represent symmetric "stress intensity factors". If the odd functions are selected from $D_b(z)$, that satisfies traction-free boundary condition at $z^* = \pm 1$, it can yield the out-of-plane bending/twisting case given by

$$D_{bj}(z) = D_{ba\,j}(z) = D_{1\,j}\sin(\alpha z), \qquad j = 1,2 \tag{25}$$

$D_{ba\,j}(z)$ that satisfies the singular-stress-free conditions on the cracked bicrystalline superlattice plate surfaces is given by

$$D_{baj}(z) = \sum_{m=1}^{\pm\infty} D_{2mj}\sin(m\pi z^*), \qquad j = 1,2, \tag{26}$$

Here $K_I = K_{Ia}$ and $K_{II} = K_{IIa}$ are anti-symmetric stress intensity factors. Eqs. (25) and (26) are valid, provided the loading function vanishes at $z^* = 0$, thus eliminating the possibility of discontinuity of the function at $z^* = 0$. In the presence of discontinuity of the function at $z^* = 0$, $D_{bja}(z)$ can be written as follows:

$$D_{baj}(z) = \left|\sum_{m=0}^{\pm\infty} D_{1mj}\cos\left(\frac{(2m+1)\pi z^*}{2}\right)\right|, \qquad j = 1,2 \tag{27}$$

If the singular-stress-free boundary conditions, given by Eqs. (3) on the cracked bicrystalline superlattice plate surfaces are satisfied, all the displacements also vanish on these surfaces in the vicinity of the front of a bicrystalline interface crack.

6.2. Hyperbolic Sine Distributed Far-Field Loading

Hyperbolic sine distributed far-field loading, which is proportional to $\sinh(z^*)$, $|z^*| < 1$, is applied. The applied antisymmetric loading function and the corresponding "stress intensity factors" (valid for $|\tilde{z}^*| \le 1$) are proportional to

$$D_{ba}(z^*) = \sinh(z^*) = \frac{\exp(z^*) - \exp(-z^*)}{2}. \tag{28}$$

The corresponding Fourier series can be derived as follows:

$$D_{ba}(z^*) = \sum_{m=0}^{\infty} \frac{\left\{e^{-1}(-1)^m - e(-1)^m\right\}}{\left\{1 + m^2\pi^2\right\}} m\pi\sin(m\pi z^*). \tag{29}$$

The applied symmetric loading function (valid for $|z^*| < 1$) and the corresponding "stress intensity factors" (valid for $|z^*| \le 1$) are proportional to

$$D_{bs}(z^*) = |\sinh(-z)| = \frac{1}{2}\left|\exp(z^*) - \exp(-z^*)\right|. \tag{30}$$

The corresponding Fourier series can be obtained as given below:

$$D_{bs}(z^*) = \left|\sum_{m=0}^{\infty} \frac{\left\{e^{-1}(-1)^m - e(-1)^m\right\}}{\left\{1 + m^2\pi^2\right\}} m\pi\sin(m\pi z^*)\right|. \tag{31}$$

 doi:10.20944/preprints202403.1319.v1

Alternatively, since $D_{bs}\left(z^*\right)$ has no discontinuity at z^* = 0,, it can also be derived as given below:

$$D_{bs}\left(z^*\right)=\sum_{m=0}^{\infty}\frac{\left\{e^{-1}(-1)^m-e(-1)^m\right\}}{\left\{1+\left(m+\frac{1}{2}\right)^2\pi^2\right\}}\left(m+\frac{1}{2}\right)\pi\cos\left(\left(\frac{2m+1}{2}\right)\pi z^*\right). \tag{32}$$

7. Singular Stress Fields in the Vicinity of a Through-Crack Front Propagating under Mode III (Anti-plane Shear) in [100] Direction

Yoon and Chaudhuri [54] have already addressed the problem of a cracked tri-crystal plate subjected to mode III (anti-plane shear loading). The present problem is a special case of that, and can be obtained by substituting $q_1 = p$ (refer to Figure 1 of Yoon and Chaudhuri [54]).

8. Crack Path Stability/Instability Criteria

8.1. Necessary Condition —— Griffith-Irwin theory-based crack deflection criterion

The important issue of a cleavage plane being deemed easy or difficult can be related to a crack deflection criterion, which is based on the relative fracture energy (or the energy release rate) available for possible fracture pathways [14]. The deflection or kinking of a crack from the cleavage system 1 to the cleavage system 2 is favored if (however. not iff, i.e., if and only if):

$$G_1/(2\Gamma_1)<1<G_2/(2\Gamma_2)\Rightarrow \quad G_2/G_1>\Gamma_2/\Gamma_1, \tag{33}$$

in which G_j and G_j, j = 1, 2, are energy release rate (fracture energy) and surface energy, respectively, of the j^{th} cleavage system.

It may be noted here that experimental determination of critical surface energy, G_j, j = 1, 2, of the component phase or the corresponding interfacial energy, G_{int}, of a bicrystalline superlattice can sometimes be notoriously challenging, due to the presence of micro-to-nano scale defects, such as porosity, dislocation, twin boundaries, misalignment of bonds with respect to the loading axis, and the like. In contrast, the bond shear strain at superlattice crack deflection, γ_{bd}^{s}, and superlattice crack deflection (SCD) barrier, ΔK^{s*}, to be discussed below, are, relatively speaking, much easier in comparison to determination of the critical surface or interfacial energy.

8.2. Sufficient Condition

The above Griffith-Irwin theory-based crack deflection criterion condition (albeit being still very useful and widely employed) is not accepted as a sufficient condition for a cleavage system deemed to be easy or difficult for crack propagation in single crystals [60], the most enigmatic being the {100} cleavage of BCC transition metals, especially macroscopically isotropic tungsten (W). Although the close packed {110} surface has lower surface energy, the preferred cleavage plane has experimentally been observed by Hull et al. [61] to be {100} (see also Riedle et al. [60]). For W, {100}⟨001⟩ ({crack plane}<crack front>) is deemed to be the preferred cleavage system for reasons of having d^2sp^3 hybridized orbitals, while {-110}<001> is considered to be difficult for crack propagation.

Atomistic scale modeling of cracks requires consideration of both the long-range elastic interactions and the short-range chemical reactions. The Griffith theory does not take the latter into account [49]. Secondly and more importantly, fracture criteria derived from equilibrium theories such as the Griffith (thermodynamics-based) energy balance criterion is not equipped to meet the sufficiency condition, because of the prevailing non-equilibrium conditions such as physico-chemical reactions during crack propagation. Hence, such criteria can only be regarded as necessary conditions for fracture, but not as sufficient [60,62]. The effect of short-range chemical reactions can obviously be encapsulated by atomic scale simulations, such as the investigation of low-speed propagation instabilities in silicon using quantum-mechanical hybrid, multi-scale modelling due to Kermode et al. [62], which, however, entails extensive computational and other resources. Alternatively, and

 doi:10.20944/preprints202403.1319.v1

more importantly, such short-range interactions can also be captured by the elastic properties-based parameters (with a few exceptions), such as the planar anisotropic ratio, A_j, or equivalently, the normalized elastic parameter, k_j, j = 1, 2 [49]. General theory behind these characteristics pertaining to structural chemistry of crystals are available in well-known treatises (see e.g., [64–66]). More specifically, the elastic properties of superconducting $YBa_2Cu_3O_{7-d}$ are strongly influenced by oxygen non-stoichiometry (as well as various structural defects).

A single dimensionless parameters, such as the planar anisotropic ratio, A_j, or equivalently, the normalized elastic parameter, k_j, j = 1, 2, can serve as the Holy Grail quantity for an *a priori* determination of the status of a cleavage system to be easy or difficult, very much akin to Reynold's number for fluid flow problems, crossing a critical value of which signifies transition from one regime to another. Here, the planar anisotropic ratio, A_j, or equivalently, normalized elastic parameter, k_j, j = 1, 2, for a (010)[001]×[100] cleavage system, crossing the critical value of 1 or $\sqrt{c_{22}^{(j)} / c_{11}^{(j)}}$, j = 1, 2, respectively, signifies transitioning from self-similar crack growth or propagation to crack deflection or turning from a difficult cleavage system onto a nearby easy one. This is a significant qualitative as well as quantitative improvement over two-parameters based models, suggested by earlier researchers e.g. [13], in the context of two-dimensional anisotropic fracture mechanics.

Finally, just as the introduction of Reynold's number facilitated design and setting up of experiments in addition to experimental verification of analytical and computational solutions in fluid dynamics, the accuracy and efficacy of the available experimental results on elastic constants of monocrystalline superconducting $YBa_2Cu_3O_{7-d}$, measured by modern experimental techniques with resolutions at the atomic scale or nearly so, such as X-Ray diffraction [67], ultrasound technique [68–70], neutron diffraction [71]/scattering [72], Brillouin spectroscopy [73,74]/scattering [75], resonant ultrasound spectroscopy [76,77] and the like, in a way best suited to preserve the characteristics associated with short-range interactions [59], is assessed with a powerful theoretical analysis on crack path stability/instability, in part based on a single dimensionless parameter, such as the planar anisotropic ratio, A_j, or equivalently, the normalized elastic parameter, k_j, j = 1, 2.

9. Numerical Results and Discussions

9.1. Structure-Fracture Property Relations for Certain Model Bicrystalline Superlattices

In what follows, 22 model bicrystal (superlattice) cleavage systems, each comprising a nano-film deposited on a substrate, are investigated. Table 1 lists the structures and elastic stiffness constants (with respect to <100> axes) of these mono-crystalline materials. Tables 2–19 list the cleavage systems, (crack plane)[crack front]x[initial propagation direction], and elastic stiffness constants (with respect suitably rotated coordinates) of the component phases of the bicrystalline superlattice systems 1-22. For example, the hexagonal substrate or material 2 is rotated such that $\{11\bar{2}0\}$ (a prism plane) is parallel to the crack face. It may be noted that the rotated crystal displays tetragonal type symmetry.

Table 1. Structures and elastic properties of various single crystals.

Single Crystal	Bravais Lattice	Structure	C_{11} (GPa)	C_{22} (GPa)	C_{33} (GPa)	C_{12} (GPa)	C_{13} (GPa)	C_{23} (GPa)	C_{44} (GPa)	C_{55} (GPa)	C_{66} (GPa)
Au [78]	FCC	FCC	192.9	192.9	192.9	163.8	163.8	163.8	41.5	41.5	41.5
MgO [78]	FCC	Rock Salt	289.3	289.3	289.3	87.70	87.70	87.70	154.77	154.77	154.77
$SrTiO_3$ [78]	Simple Cubic	Perovskite	348.17	348.17	348.17	100.64	100.64	100.64	454.55	454.55	454.55
Si_3N_4	HCP	HCP	343.0	343.0	600.0	136.0	120.0	120.0	124.0	124.0	103.5
$YBa_2C_3O_7$ [72]*	Tetra-gonal	Perovskite	230.0	230.0	150.0	100.0	100.0	100.0	50.0	50.0	85.0

 doi:10.20944/preprints202403.1319.v1

$YBa_2C_3O_{7-d}$ [59,70,76] †	Ortho-rhombic	Perovskite	231.0	268.0	186.0	66.0	71.0	95.0	49.0	37.0	82.0

* All values measured by neutron scattering by Reichardt et al. [72]. †All values measured by resonant ultrasound spectroscopy by Lei et al. [76] except C_{12} and C_{66} measured by ultrasound by Saint-Paul and Henry [70.

Table 2. Cleavage system: (crack plane)[crack front]x[initial propagation direction], and elastic stiffness constants of the component phases of the bicrystalline superlattice system 1.

Material (j) #	Single Crystal Phase	Cleavage System	c'_{11} (GPa)	c'_{22} (GPa)	c'_{33} (GPa)	c'_{12} (GPa)	c'_{13} (GPa)	c'_{23} (GPa)	c'_{44} (GPa)	c'_{55} (GPa)	c'_{66} (GPa)
1	Au (FCC)	(010)[001] x[100]	192.9	192.9	192.9	163.8	163.8	163.8	41.5	41.5	41.5
2*	Si_3N_4 (HCP)	(001)[0 $\bar{1}$ 0] x[$\bar{1}$ 00]	343.0	600.0	343.0	120.0	136.0	120.0	124.0	103.5	124.0

*Rotated about z-axis by 90°, then rotated about the new x-axis by -90°.

Table 3. Cleavage system: (crack plane)[crack front]x[initial propagation direction], and elastic stiffness constants of the component phases of the bicrystalline superlattice system 2.

Material (j) #	Single Crystal Phase	Cleavage System	c'_{11} (GPa)	c'_{22} (GPa)	c'_{33} (GPa)	c'_{12} (GPa)	c'_{13} (GPa)	c'_{23} (GPa)	c'_{44} (GPa)	c'_{55} (GPa)	c'_{66} (GPa)
1	Au (FCC)	(010)[001] x[100]	192.9	192.9	192.9	163.8	163.8	163.8	41.5	41.5	41.5
2*	Si_3N_4 (HCP)	($\bar{1}$ 00)[0 $\bar{1}$ 0] x[001]	600.0	343.0	343.0	120.0	120.0	136.0	103.5	124.0	124.0

*Rotated first about y-axis by -90°, then rotated about the new x-axis by 90°.

Table 4. Cleavage system: (crack plane)[crack front]x[initial propagation direction], and elastic stiffness constants of the component phases of the bicrystalline superlattice system 3.

Material (j) #	Single Crystal Phase	Cleavage System	c'_{11} (GPa)	c'_{22} (GPa)	c'_{33} (GPa)	c'_{12} (GPa)	c'_{13} (GPa)	c'_{23} (GPa)	c'_{44} (GPa)	c'_{55} (GPa)	c'_{66} (GPa)
1	Au (FCC)	($\bar{1}$ 10)[001] x[110]	219.85	219.85	192.9	136.85	163.8	163.8	41.5	41.5	14.5
2*	Si_3N_4 (HCP)	(001)[0 $\bar{1}$ 0] x[$\bar{1}$ 00]	343.0	600.0	343.0	120.0	136.0	120.0	124.0	103.5	124.0

*Rotated about z-axis by 90°, then rotated about the new x-axis by -90°.

Table 5. Cleavage system: (crack plane)[crack front]x[initial propagation direction], and elastic stiffness constants of the component phases of the bicrystalline superlattice system 4.

Material (j) #	Single Crystal Phase	Cleavage System	c'_{11} (GPa)	c'_{22} (GPa)	c'_{33} (GPa)	c'_{12} (GPa)	c'_{13} (GPa)	c'_{23} (GPa)	c'_{44} (GPa)	c'_{55} (GPa)	c'_{66} (GPa)
1	Au (FCC)	($\bar{1}$ 10)[001] x[110]	219.85	219.85	192.9	136.85	163.8	163.8	41.5	41.5	14.5

 doi:10.20944/preprints202403.1319.v1

2*	Si_3N_4 (HCP)	$(\bar{1}00)[0\bar{1}0]$ x[001]	600.0	343.0	343.0	120.0	120.0	136.0	103.5	124.0	124.0

*Rotated first about y-axis by -90°, then rotated about the new x-axis by 90°.

Table 6. Cleavage system: (crack plane)[crack front]x[initial propagation direction], and elastic stiffness constants of the component phases of the bicrystalline superlattice system 5.

Material (j) #	Single Crystal Phase	Cleavage System	c'_{11} (GPa)	c'_{22} (GPa)	c'_{33} (GPa)	c'_{12} (GPa)	c'_{13} (GPa)	c'_{23} (GPa)	c'_{44} (GPa)	c'_{55} (GPa)	c'_{66} (GPa)
1	Au (FCC)	(010)[001]x[100]	192.9	192.9	192.9	163.8	163.8	163.8	41.5	41.5	41.5
2	MgO (FCC)	(010)[001]x[100]	289.3	289.3	289.3	87.7	87.7	87.7	154.77	154.77	154.77

Table 7. Cleavage system: (crack plane)[crack front]x[initial propagation direction], and elastic stiffness constants of the component phases of the bicrystalline superlattice system 6.

Material (j) #	Single Crystal Phase	Cleavage System	c'_{11} (GPa)	c'_{22} (GPa)	c'_{33} (GPa)	c'_{12} (GPa)	c'_{13} (GPa)	c'_{23} (GPa)	c'_{44} (GPa)	c'_{55} (GPa)	c'_{66} (GPa)
1	Au (FCC)	(010)[001] x[100]	192.9	192.9	192.9	163.8	163.8	163.8	41.5	41.5	41.5
2	MgO (FCC)	$(\bar{1}10)[001]$ x[110]	343.27	343.27	289.3	33.73	87.7	87.7	154.77	154.77	100.8

Table 8. Cleavage system: (crack plane)[crack front]x[initial propagation direction], and elastic stiffness constants of the component phases of the bicrystalline superlattice system 7.

Material (j) #	Single Crystal Phase	Cleavage System	c'_{11} (GPa)	c'_{22} (GPa)	c'_{33} (GPa)	c'_{12} (GPa)	c'_{13} (GPa)	c'_{23} (GPa)	c'_{44} (GPa)	c'_{55} (GPa)	c'_{66} (GPa)
1	Au (FCC)	$(\bar{1}10)[001]$ x[110]	219.85	219.85	192.9	136.85	163.8	163.8	41.5	41.5	14.5
2	MgO (FCC)	(010)[001]x[100]	289.3	289.3	289.3	87.7	87.7	87.7	154.77	154.77	154.77

Table 9. Cleavage system: (crack plane)[crack front]x[initial propagation direction], and elastic stiffness constants of the component phases of the bicrystalline superlattice system 8.

Material (j) #	Single Crystal Phase	Cleavage System	c'_{11} (GPa)	c'_{22} (GPa)	c'_{33} (GPa)	c'_{12} (GPa)	c'_{13} (GPa)	c'_{23} (GPa)	c'_{44} (GPa)	c'_{55} (GPa)	c'_{66} (GPa)
1	Au (FCC)	$(\bar{1}10)[001]$ x[110]	219.85	219.85	192.9	136.85	163.8	163.8	41.5	41.5	14.5
2	MgO (FCC)	$(\bar{1}10)[001]$ x[110]	343.27	343.27	289.3	33.73	87.7	87.7	154.77	154.77	100.8

 doi:10.20944/preprints202403.1319.v1

Table 10. Cleavage system (crack plane)[crack front]x[initial propagation direction], and elastic stiffness constants of the component phases of the bicrystalline superlattice system 9.

Material (j) #	Single Crystal Phase	Cleavage System	c'_{11} (GPa)	c'_{22} (GPa)	c'_{33} (GPa)	c'_{12} (GPa)	c'_{13} (GPa)	c'_{23} (GPa)	c'_{44} (GPa)	c'_{55} (GPa)	c'_{66} (GPa)
1	$YBa_2C_3O_7$ (Tetra-gonal)	(010)[001] x[100]	230.0	230.0	150.0	100.0	100.0	100.0	50.0	50.0	85.0
2*	Si_3N_4 (HCP)	$(\bar{1}\,00)[0\,\bar{1}\,0]$ x[001]	600.0	343.0	343.0	120.0	120.0	136.0	103.5	124.0	124.0

*Rotated first about y-axis by -90°, then rotated about the new x-axis by 90°.

Table 11. Cleavage system (crack plane)[crack front]x[initial propagation direction], and elastic stiffness constants of the component phases of the bicrystalline superlattice system 10.

Material (j) #	Single Crystal Phase	Cleavage System	c'_{11} (GPa)	c'_{22} (GPa)	c'_{33} (GPa)	c'_{12} (GPa)	c'_{13} (GPa)	c'_{23} (GPa)	c'_{44} (GPa)	c'_{55} (GPa)	c'_{66} (GPa)
1	$YBa_2C_3O_7$ (Tetra-gonal)	(010)[001]x[100]	230.0	230.0	150.0	100.0	100.0	100.0	50.0	50.0	85.0
2	$SrTiO_3$ (Simple Cubic)	(010)[001]x[100]	348.17	348.17	348.17	100.64	100.64	100.64	454.55	454.55	454.55

Table 12. Cleavage system (crack plane)[crack front]x[initial propagation direction], and elastic stiffness constants of the component phases of the bicrystalline superlattice system 11.

Material (j) #	Single Crystal Phase	Cleavage System	c'_{11} (GPa)	c'_{22} (GPa)	c'_{33} (GPa)	c'_{12} (GPa)	c'_{13} (GPa)	c'_{23} (GPa)	c'_{44} (GPa)	c'_{55} (GPa)	c'_{66} (GPa)
1	$YBa_2C_3O_7$ (Tetra-gonal)	(010)[001] x[100]	230.0	230.0	150.0	100.0	100.0	100.0	50.0	50.0	85.0
2	$SrTiO_3$ (Simple Cubic)	$(\bar{1}\,10)[001]$ x[110]	678.96	678.96	348.17	-230.15	100.64	100.64	454.55	454.55	123.77

Table 13. Cleavage system (crack plane)[crack front]x[initial propagation direction], and elastic stiffness constants of the component phases of the bicrystalline superlattice system 12.

Material (j) #	Single Crystal Phase	Cleavage System	c'_{11} (GPa)	c'_{22} (GPa)	c'_{33} (GPa)	c'_{12} (GPa)	c'_{13} (GPa)	c'_{23} (GPa)	c'_{44} (GPa)	c'_{55} (GPa)	c'_{66} (GPa)
1	$YBa_2C_3O_7$ (Tetra-gonal)	$(\bar{1}\,10)[001]$ x[110]	250.0	250.0	150.0	80.0	100.0	100.0	50.0	50.0	65.0
2	$SrTiO_3$ (Simple Cubic)	$(\bar{1}\,10)[001]$ x[110]	678.96	678.96	348.17	-230.15	100.64	100.64	454.55	454.55	123.77

 doi:10.20944/preprints202403.1319.v1

Table 14. Cleavage system (crack plane)[crack front]x[initial propagation direction], and elastic stiffness constants of the component phases of the bicrystalline superlattice system 13.

Material (j) #	Single Crystal Phase	Cleavage System	c'_{11} (GPa)	c'_{22} (GPa)	c'_{33} (GPa)	c'_{12} (GPa)	c'_{13} (GPa)	c'_{23} (GPa)	c'_{44} (GPa)	c'_{55} (GPa)	c'_{66} (GPa)
1	$YBa_2C_3O_7$ (Tetra-gonal)	$(\bar{1}10)[001]$ x[110]	250.0	250.0	150.0	80.0	100.0	100.0	50.0	50.0	65.0
2	$SrTiO_3$ (Simple Cubic)	(010)[001]x[100]	348.17	348.17	348.17	100.64	100.64	100.64	454.55	454.55	454.55

Table 15. Cleavage system: (crack plane)[crack front]x[initial propagation direction], and elastic stiffness constants of the component phases of the bicrystalline superlattice system 14.

Mater-ial (j) #	Single Crystal Phase	Cleavage System	c'_{11} (GPa)	c'_{22} (GPa)	c'_{33} (GPa)	c'_{12} (GPa)	c'_{13} (GPa)	c'_{23} (GPa)	c'_{44} (GPa)	c'_{55} (GPa)	c'_{66} (GPa)
1	$YBa_2C_3O_{7-d}$ (Ortho-rhombic)	(001)[100] x[010]	268.0	186.0	231.0	95.0	66.0	71.0	37.0	82.0	49.0
2*	Si_3N_4 (HCP)	$(001)[0\ \bar{1}\ 0]$ x$[\bar{1}00]$	343.0	600.0	343.0	120.0	136.0	120.0	124.0	103.5	124.0

*Rotated about z-axis by 90°, then rotated about the new x-axis by -90°.

Table 16. Cleavage system: (crack plane)[crack front]x[initial propagation direction], and elastic stiffness constants of the component phases of the bicrystalline superlattice system 15.

Material (j) #	Single Crystal Phase	Cleavage System	c'_{11} (GPa)	c'_{22} (GPa)	c'_{33} (GPa)	c'_{12} (GPa)	c'_{13} (GPa)	c'_{23} (GPa)	c'_{44} (GPa)	c'_{55} (GPa)	c'_{66} (GPa)
1	$YBa_2C_3O_{7-d}$ (Ortho-rhombic)	(001)[100] x[010]	268.0	186.0	231.0	95.0	66.0	71.0	37.0	82.0	49.0
2	MgO (FCC)	(010)[001]x[100]	289.3	289.3	289.3	87.7	87.7	87.7	154.77	154.77	154.77

Table 17. Cleavage system: (crack plane)[crack front]x[initial propagation direction], and elastic stiffness constants of the component phases of the bicrystalline superlattice system 16.

Material (j) #	Single Crystal Phase	Cleavage System	c'_{11} (GPa)	c'_{22} (GPa)	c'_{33} (GPa)	c'_{12} (GPa)	c'_{13} (GPa)	c'_{23} (GPa)	c'_{44} (GPa)	c'_{55} (GPa)	c'_{66} (GPa)
1	$YBa_2C_3O_{7-d}$ (Ortho-rhombic)	(001)[100] x[010]	268.0	186.0	231.0	95.0	66.0	71.0	37.0	82.0	49.0
2	MgO (FCC)	$(\bar{1}10)[001]$ x[110]	343.27	343.27	289.3	33.73	87.7	87.7	154.77	154.77	100.8

 doi:10.20944/preprints202403.1319.v1

Table 18. Cleavage system (crack plane)[crack front]x[initial propagation direction], and elastic stiffness constants of the component phases of the bicrystalline superlattice system 17.

Material (j) #	Single Crystal Phase	Cleavage System	c'_{11} (GPa)	c'_{22} (GPa)	c'_{33} (GPa)	c'_{12} (GPa)	c'_{13} (GPa)	c'_{23} (GPa)	c'_{44} (GPa)	c'_{55} (GPa)	c'_{66} (GPa)
1	$YBa_2C_3O_{7-d}$ (Ortho-rhombic)	(001)[100]x[010]	268.0	186.0	231.0	95.0	66.0	71.0	37.0	82.0	49.0
2	$SrTiO_3$ (Simple Cubic)	(010)[001]x[100]	348.17	348.17	348.17	100.64	100.64	100.64	454.55	454.55	454.55

Table 19. Cleavage system (crack plane)[crack front]x[initial propagation direction], and elastic stiffness constants of the component phases of the bicrystalline superlattice system 18.

Material (j) #	Single Crystal Phase	Cleavage System	c'_{11} (GPa)	c'_{22} (GPa)	c'_{33} (GPa)	c'_{12} (GPa)	c'_{13} (GPa)	c'_{23} (GPa)	c'_{44} (GPa)	c'_{55} (GPa)	c'_{66} (GPa)
1	$YBa_2C_3O_{7-d}$ (Ortho-rhombic)	(001)[100]x[010]	268.0	186.0	231.0	95.0	66.0	71.0	37.0	82.0	49.0
2	$SrTiO_3$ (Simple Cubic)	$(\bar{1}10)$[001]x[110]	678.96	678.96	348.17	-230.15	100.64	100.64	454.55	454.55	123.77

The bicrystalline superlattice systems investigated here are namely as follows: (i) Au (gold), nano-layer/film or material 1 deposited on Si_3N_4 (silicon nitride), substrate or material 2 (Tables 2–5), (ii) Au (nano-layer/film) deposited on substrate MgO (magnesium oxide) (Tables 6–9), (iii) $YBa_2C_3O_7$ (tetragonal/fully oxidized or non-superconducting $YBa_2Cu_3O_7$, in short $YBCO^T$) nano-layer/film, deposited on substrate Si_3N_4 (Table 10), (iv) $YBa_2C_3O_7$ (nano-layer/film) deposited on substrate, $SrTiO_3$ (Tables 11–14), (v) $YBa_2C_3O_{7-d}$ (superconducting YBCO, in short YBCO) nano-layer/film, deposited on substrate Si_3N_4 (Table 15), (vi) $YBa_2C_3O_{7-d}$, nano-layer/film deposited on substrate MgO (Tables 16, 17), and (vii) $YBa_2C_3O_{7-d}$ (nano-layer/film) deposited on substrate, $SrTiO_3$ (strontium titanate) (Tables 18–23),. For the bicrystalline superlattice systems under investigation, the computed mode I, II, or mixed mode I/II order of stress singularity, $\lambda_i = 1 - s_i$, i = 1, 2, is found to be 0.5±ie or o.5. In contrast, the computed mode III order of stress singularity, $\lambda_3 = 1 - s_3$, is always equal to 0.5.

Table 20. Cleavage system (crack plane)[crack front]x[initial propagation direction], and elastic stiffness constants of the component phases of the bicrystalline superlattice system 19.

Material (j) #	Single Crystal Phase	Cleavage System	c'_{11} (GPa)	c'_{22} (GPa)	c'_{33} (GPa)	c'_{12} (GPa)	c'_{13} (GPa)	c'_{23} (GPa)	c'_{44} (GPa)	c'_{55} (GPa)	c'_{66} (GPa)
1	$YBa_2C_3O_{7-d}$ (Ortho-rhombic)	010)[001]x[100]	231.0	268.0	186.0	66.0	71.0	95.0	49.0	37.0	82.0
2	$SrTiO_3$ (Simple Cubic)	(010)[001]x[100]	348.17	348.17	348.17	100.64	100.64	100.64	454.55	454.55	454.55

 doi:10.20944/preprints202403.1319.v1

Table 21. Cleavage system (crack plane)[crack front]x[initial propagation direction], and elastic stiffness constants of the component phases of the bicrystalline superlattice system 20.

Material (j) #	Single Crystal Phase	Cleavage System	c'_{11} (GPa)	c'_{22} (GPa)	c'_{33} (GPa)	c'_{12} (GPa)	c'_{13} (GPa)	c'_{23} (GPa)	c'_{44} (GPa)	c'_{55} (GPa)	c'_{66} (GPa)
1	$YBa_2C_3O_{7-d}$ (Ortho-rhombic)	(010)[001] x[100]	231.0	268.0	186.0	66.0	71.0	95.0	49.0	37.0	82.0
2	$SrTiO_3$ (Simple Cubic)	$(\bar{1}10)$[001] x[110]	678.96	678.96	348.17	-230.15	100.64	100.64	454.55	454.55	123.77

Table 22. Cleavage system (crack plane)[crack front]x[initial propagation direction], and elastic stiffness constants of the component phases of the bicrystalline superlattice system 21.

Material (j) #	Single Crystal Phase	Cleavage System	c'_{11} (GPa)	c'_{22} (GPa)	c'_{33} (GPa)	c'_{12} (GPa)	c'_{13} (GPa)	c'_{23} (GPa)	c'_{44} (GPa)	c'_{55} (GPa)	c'_{66} (GPa)
1	$YBa_2C_3O_{7-d}$ (Ortho-rhombic)	$(\bar{1}00)$[001] x[010]	268.0	231.0	186.0	66.0	95.0	71.0	37.0	49.0	82.0
2	$SrTiO_3$ (Simple Cubic)	(010)[001]x[100]	348.17	348.17	348.17	100.64	100.64	100.64	454.55	454.55	454.55

Table 23. Cleavage system (crack plane)[crack front]x[initial propagation direction], and elastic stiffness constants of the component phases of the bicrystalline superlattice system 22.

Material (j) #	Single Crystal Phase	Cleavage System	c'_{11} (GPa)	c'_{22} (GPa)	c'_{33} (GPa)	c'_{12} (GPa)	c'_{13} (GPa)	c'_{23} (GPa)	c'_{44} (GPa)	c'_{55} (GPa)	c'_{66} (GPa)
1	$YBa_2C_3O_{7-d}$ (Ortho-rhombic)	$(\bar{1}00)$[001] x[010]	268.0	231.0	186.0	66.0	95.0	71.0	37.0	49.0	82.0
2	$SrTiO_3$ (Simple Cubic)	$(\bar{1}10)$[001] x[110]	678.96	678.96	348.17	-230.15	100.64	100.64	454.55	454.55	123.77

In the FCC metal nano-film, Au, listed in Tables 2–9 and Tables 24–31, all the orbitals belong to the d-block with partially filled d-shells [66]. In a monocrystalline FCC metal, the bonds are oriented along the face diagonals, <110>. Such a metal contains linear chains of near-neighbor bonds in these directions, resulting in higher elastic stiffness constants along them. As shown in Tables 20, 25, 28 and 29, A = 2.8522 > 1, and k = 4.9777 > $\sqrt{c_{22}/c_{11}}$ = 1 for Au, giving rise to complex roots for a {010}<001>x<100> through-crack. Similar calculations yield A' = 0.3494 < 1, and κ' = 0.2487 < $\sqrt{c'_{22}/c'_{11}}$ = 1 for Au, giving rise to imaginary roots for the $\{\bar{1}10\}$<001>x<110> through-crack [49], as can be seen from Tables 26, 27, 30 and 31. It can then be inferred that $\{\bar{1}10\}$<001>x<110> would constitute an easy cleavage system, while {010}<001>x<100> would be deemed difficult.

 doi:10.20944/preprints202403.1319.v1

Table 24. Normalized elastic parameter, roots of characteristic equation, and the nature (easy or difficult) of the through-thickness cleavage system of the bicrystalline superlattice system 1.

Material (j) #	Cleavage System	A'	$\sqrt{\frac{c'_{22}}{c'_{11}}}$	κ'	Roots	Cleavage System: Easy or Difficult
Au (FCC)	(010)[001]x[100]	2.8522	1.0	4.9777	Complex	Difficult
Si_3N_4 (HCP)	(001)[0 $\bar{1}$ 0] x[$\bar{1}$ 00]	0.7433	1.3226	0.9206	Imaginary	Easy

Table 25. Normalized elastic parameter, roots of characteristic equation, and the nature (easy or difficult) of the through-thickness cleavage system of the bicrystalline superlattice system 2 .

Material (j) #	Cleavage System	A'	$\sqrt{\frac{c'_{22}}{c'_{11}}}$	κ'	Roots	Cleavage System: Easy or Difficult
Au (FCC)	(010)[001] x[100]	2.8522	1.0	4.9777	Complex	Difficult
Si_3N_4 (HCP)	($\bar{1}$ 00)[0 $\bar{1}$ 0] x[001]	0.7433	0.5717	0.5263	Imaginary	Easy

Table 26. Normalized elastic parameter, roots of characteristic equation, and the nature (easy or difficult) of the through-thickness cleavage system of the bicrystalline superlattice system 3 .

Material (j) #	Cleavage System	A'	$\sqrt{\frac{c'_{22}}{c'_{11}}}$	κ'	Roots	Cleavage System: Easy or Difficult
Au (FCC)	($\bar{1}$ 10)[001] x[110]	0.3494	1.0	0.2487	Imaginary	Easy
Si_3N_4 (HCP)	(001)[0 $\bar{1}$ 0] x[$\bar{1}$ 00]	0.7433	1.3226	0.9206	Imaginary	Easy

Table 27. Normalized elastic parameter, roots of characteristic equation, and the nature (easy or difficult) of the through-thickness cleavage system of the bicrystalline superlattice system 4.

Material (j) #	Cleavage System	A'	$\sqrt{\frac{c'_{22}}{c'_{11}}}$	κ'	Roots	Cleavage System: Easy or Difficult
Au (FCC)	($\bar{1}$ 10)[001] x[110]	0.3494	1.0	0.2487	Imaginary	Easy
Si_3N_4 (HCP)	($\bar{1}$ 00)[0 $\bar{1}$ 0] x[001]	0.7433	0.5717	0.5263	Imaginary	Easy

Table 28. Normalized elastic parameter, roots of characteristic equation, and the nature (easy or difficult) of the through-thickness cleavage system of the bicrystalline superlattice system 5 .

Material (j) #	Cleavage System	A'	$\sqrt{\frac{c'_{22}}{c'_{11}}}$	κ'	Roots	Cleavage System: Easy or Difficult
Au (FCC)	(010)[001]x[100]	2.8522	1.0	4.9777	Complex	Difficult
MgO (FCC)	(010)[001]x[100]	1.5354	1.0	1.8329	Complex	Difficult

Table 29. Normalized elastic parameter, roots of characteristic equation, and the nature (easy or difficult) of the through-thickness cleavage system of the bicrystalline superlattice system 6.

 doi:10.20944/preprints202403.1319.v1

Material (j) #	Cleavage System	A'	$\sqrt{\frac{c'_{22}}{c'_{11}}}$	κ'	Roots	Cleavage System: Easy or Difficult
Au (FCC)	(010)[001]x[100]	2.8522	1.0	4.9777	Complex	Difficult
MgO (FCC)	$(\bar{1}10)$[001] x[110]	0.6513	1.0	0.6297	Imaginary	Easy

Table 30. Normalized elastic parameter, roots of characteristic equation, and the nature (easy or difficult) of the through-thickness cleavage system of the bicrystalline superlattice system 7.

Material (j) #	Cleavage System	A'	$\sqrt{\frac{c'_{22}}{c'_{11}}}$	κ'	Roots	Cleavage System: Easy or Difficult
Au (FCC)	$(\bar{1}10)$[001] x[110]	0.3494	1.0	0.2487	Imaginary	Easy
MgO (FCC)	(010)[001] x[100]	1.5354	1.0	1.8329	Complex	Difficult

Table 31. Normalized elastic parameter, roots of characteristic equation, and the nature (easy or difficult) of the through-thickness cleavage system of the bicrystalline superlattice system 8 .

Material (j) #	Cleavage System	A'	$\sqrt{\frac{c'_{22}}{c'_{11}}}$	κ'	Roots	Cleavage System: Easy or Difficult
Au (FCC)	$(\bar{1}10)$[001] x[110]	0.3494	1.0	0.2487	Imaginary	Easy
MgO (FCC)	$(\bar{1}10)$[001] x[110]	0.6513	1.0	0.6297	Imaginary	Easy

The ionic crystal MgO (an alkaline earth metal oxide), used as a substrate, which is listed in Tables 6–9, 16 and 17, in addition to in Tables 28–31, 38 and 39, is a structurally of rock salt type, but is an exception to the general rule for ionic crystals, such as alkali halides (e.g., NaCl and KCl), with the rock salt structure [49,64]. The reason is, as explained by Newnham [64], due to Mg^{2+} (and also Li^{+}) being small cations, which permit the anions to be in contact with one another and consequently, restrict bending actions. As a result, elastic stiffness coefficients in the <110> and <111> directions become larger than their <100> counterparts. This is in contrast to NaCl and KCl, wherein Cl^{-} anions are not in contact. Additionally, the importance of anion-anion forces were pointed out by Weidner and Simmons [79]. These researchers have found, in connection with the computation of elastic properties of several alkali halides from a two-body central force model, the necessity to include anion-anion interactions in addition to cation-anion forces. As shown in Tables 29, 31 and 39, A' = 0.6513 and κ' = 0.6297 are both less than unity (A' < 1, κ' < $\sqrt{c'_{22}/c'_{11}}$ = 1) giving rise to imaginary roots for the $(\bar{1}10)$[001]x[110] through-crack. This is in contrast to A = 1.5354 and k = 1.8329 being both larger than unity (A > 1, k > $\sqrt{c_{22}/c_{11}}$ = 1), giving rise to complex roots for the (010)[001]x[100] through-crack, as shown in Tables 28, 30 and 38. It can then be inferred that $\{\bar{1}10\}$ <001>x<110> would constitute an easy cleavage system, while {010}<001>x<100> would be deemed difficult.

The next substrate, perovskite, Strontium titanate ($SrTiO_3$), is listed in Tables 11–14 and 18–23 as well as in Tables 33–36 and 40-45. $SrTiO_3$ has at room temperature, an ideal cubic perovskite structure with TiO_6 octahedra being connected by straight chains [63]. Tables 34, 36 and 41 show that

 doi:10.20944/preprints202403.1319.v1

A' = 0.2723 and κ' = 0.3614 are both less than unity (A' < 1, κ' < $\sqrt{c_{11}/c'_{11}}$ = 1), giving rise to imaginary roots for the ($\bar{1}$10)[001]x[110] through-crack. This is in contrast to A = 3.6727 and k = 16.1473 being both larger than unity (A > 1, k > $\sqrt{c_{22}/c_{11}}$ = 1), giving rise to complex roots for the (010)[001]x[100] through-crack, as shown in Tables 33, 35 and 40. It can then be inferred that $\{\bar{1}10\}$ <001>x<110> would constitute an easy cleavage system, while {010}<001>x<100> would be deemed difficult.

The third and last substrate studied here is hexagonal close-packed (HCP) Si_3N_4, which is listed in Tables 2–5, 10 and 15 as well as in Tables 24–27, 32 and 37. Tables 24, 26 and 32 show that A' = 0.7433 < 1 and κ' = 0.9206 < $\sqrt{c'_{22}/c'_{11}}$ = 1.3226, giving rise to imaginary roots for the (001)[0 $\bar{1}$ 0] x[$\bar{1}$ 00] through-crack. In a similar vein, A' = 0.7433 < 1 and κ' = 0.5263 < $\sqrt{c'_{22}/c'_{11}}$ = 0.5717, giving rise to imaginary roots for the ($\bar{1}$ 00)[0 $\bar{1}$ 0]x[001] through-crack, as shown in Tables 25, 27 and 37. It can then be inferred that {001}<0 $\bar{1}$ 0>x<$\bar{1}$ 00> and {$\bar{1}$ 00}<0 $\bar{1}$ 0>x<001> would both constitute easy cleavage systems.

The fully oxidized (non-superconducting) tetragonal $YBa_2C_3O_7$, the second nano-film investigated here is listed in Tables 10–14 and also in Tables 32–36. Granozio and di Uccio [83] have also presented approximate theoretical results of fully oxidized YBCO's (d = 0, 1), and concluded that the three lowest surface energies follow the inequality: ◎ (001) < g (100) < g (010). Furthermore, based on experimental results from transmission electron microscopy [84], X-ray photo-emission microscopy [85], low-energy ion scattering spectroscopy [86], and surface polarity [87] analyses performed on fully oxidized $YBa_2C_3O_7$ crystals, these authors [83] have shown that the low energy cut is between the Ba=O and Cu=O planes. Tables 32–34 show that A = 1.9077 and k = 3.1514 are both larger than unity (A > 1, k > $\sqrt{c_{22}/c_{11}}$ = 1), giving rise to complex roots for the (010)[001]x[100] through-crack. This is in contrast to A' = 0.7647 and κ' = 0.7112 being both less than unity (A' < 1, κ' < $\sqrt{c_{11}/c'_{11}}$ = 1), giving rise to imaginary roots for the ($\bar{1}$10)[001]x[110] through-crack. as shown in Tables 35 and 36. It can then be inferred that $\{\bar{1}10\}$<001>x<110> would constitute an easy cleavage system, while {010}<001>x<100> would be deemed difficult.

Table 32. Normalized elastic parameter, roots of characteristic equation, and the nature (easy or difficult) of the through-thickness cleavage system of the bicrystalline superlattice system 9 .

Material (j) #	Cleavage System	A'	$\sqrt{\frac{c'_{22}}{c'_{11}}}$	κ'	Roots	Cleavage System: Easy or Difficult
$YBa_2C_3O_7$ (Tetra-gonal)	(010)[001] x[100]	1.9077	1.0	3.1514	Complex	Difficult
Si_3N_4 (HCP)	($\bar{1}$ 00)[0 $\bar{1}$ 0] x[001]	0.7433	0.5717	0.9206	Imaginary	Easy

Table 33. Normalized elastic parameter, roots of characteristic equation, and the nature (easy or difficult) of the through-thickness cleavage system of the bicrystalline superlattice system 10.

Material (j) #	Cleavage System	A'	$\sqrt{\frac{c'_{22}}{c'_{11}}}$	κ'	Roots	Cleavage System: Easy or Difficult
$YBa_2C_3O_7$ (Tetra-gonal)	(010)[001]x[100]	1.9077	1.0	3.1514	Complex	Difficult

 doi:10.20944/preprints202403.1319.v1

$SrTiO_3$ (Simple Cubic)	(010)[001]x[100]	3.6727	1.0	16.1473	Complex	Difficult

Table 34. Normalized elastic parameter, roots of characteristic equation, and the nature (easy or difficult) of the through-thickness cleavage system of the bicrystalline superlattice system 11.

Material (j) #	Cleavage System	A'	$\sqrt{c'_{22}/c'_{11}}$	κ'	Roots	Cleavage System: Easy or Difficult
$YBa_2C_3O_7$ (Tetra-gonal)	(010)[001]x[100]	1.9077	1.0	3.1514	Complex	Difficult
$SrTiO_3$ (Simple Cubic)	$(\bar{1}\,10)[001]$ x[110]	0.2723	1.0	0.3614	Imaginary	Easy

Table 35. Normalized elastic parameter, roots of characteristic equation, and the nature (easy or difficult) of the through-thickness cleavage system of the bicrystalline superlattice system 12.

Material (j) #	Cleavage System	A'	$\sqrt{c'_{22}/c'_{11}}$	κ'	Roots	Cleavage System: Easy or Difficult
$YBa_2C_3O_7$ (Tetra-gonal)	$(\bar{1}\,10)[001]$ x[110]	0.7647	1.0	0.7112	Imaginary	Easy
$SrTiO_3$ (Simple Cubic)	(010)[001]x[100]	3.6727	1.0	16.1473	Complex	Difficult

Table 36. Normalized elastic parameter, roots of characteristic equation, and the nature (easy or difficult) of the through-thickness cleavage system of the bicrystalline superlattice system 13.

Material (j) #	Cleavage System	A'	$\sqrt{c'_{22}/c'_{11}}$	κ'	Roots	Cleavage System: Easy or Difficult
$YBa_2C_3O_7$ (Tetra-gonal)	$(\bar{1}\,10)[001]$ x[110]	0.7647	1.0	0.7112	Imaginary	Easy
$SrTiO_3$ (Simple Cubic)	$(\bar{1}\,10)[001]$ x[110]	0.2723	1.0	0.3614	Imaginary	Easy

Finally, the third nano-film, $YBa_2C_3O_{7-d}$ (orthorhombic), investigated here is a high TC superconductor, and is listed in Tables 15–23, in addition to in Tables 37–45. As can be seen from Tables 2-7 of Chaudhuri [59], all the cleavage systems are predicted to be easy, which are in agreement with the experimentally observed fracture characteristics of $YBa_2C_3O_{7-d}$ due to Cook et al. [80], Raynes et al. [81] and Goyal et al. [82] among others; see also Granozio and di Uccio [83] for a summary of the available experimental results. Here, A' = 0.764 < 1 and κ' = 0.5784 < $\sqrt{c'_{22}/c'_{11}}$ = 0.8331, giving rise to imaginary roots for the (001)[100]x[010] through-crack, as shown in Tables 37–41; see also Table 6 of Chaudhuri [59]. Similarly, A = 0.8971 < 1 and k = 0.9406 < $\sqrt{c'_{22}/c'_{11}}$ = 1.0771, giving rise to imaginary roots for the (010)[001]x[100] through-crack, as shown in Tables 42 and 43; see also Table 2 of Chaudhuri [59]. Likewise, A' = 0.8971 < 1 and κ' = 0.817 < $\sqrt{c'_{22}/c'_{11}}$ = 0.9284,

 doi:10.20944/preprints202403.1319.v1

giving rise to imaginary roots for the ($\bar{1}$ 00)[001]x[010] through-crack, as shown in Tables 44 and 45; see also Table 4 of Chaudhuri [59]. It can then be inferred that {001}<100>x<010> would constitute an easy cleavage system.

Table 37. Normalized elastic parameter, roots of characteristic equation, and the nature (easy or difficult) of the through-thickness cleavage system of the bicrystalline superlattice system 14.

Material (j) #	Cleavage System	A'	$\sqrt{\frac{c'_{22}}{c'_{11}}}$	κ'	Roots	Cleavage System: Easy or Difficult
$YBa_2C_3O_{7-d}$ (Ortho-rhombic)	(001)[100] x[010]	0.764	0.8331	0.5784	Imaginary	Easy
Si_3N_4 (HCP)	(001)[0 $\bar{1}$ 0] x[$\bar{1}$ 00]	0.7433	1.3226	0.9206	Imaginary	Easy

Table 38. Normalized elastic parameter, roots of characteristic equation, and the nature (easy or difficult) of the through-thickness cleavage system of the bicrystalline superlattice system 15.

Material (j) #	Cleavage System	A'	$\sqrt{\frac{c'_{22}}{c'_{11}}}$	κ'	Roots	Cleavage System: Easy or Difficult
$YBa_2C_3O_{7-d}$ (Ortho-rhombic)	(001)[100]x[010]	0.764	0.8331	0.5784	Imaginary	Easy
MgO (FCC)	(010)[001]x[100]	1.5354	1.0	1.8329	Complex	Difficult

Table 39. Normalized elastic parameter, roots of characteristic equation, and the nature (easy or difficult) of the through-thickness cleavage system of the bicrystalline superlattice system 16.

Material (j) #	Cleavage System	A'	$\sqrt{\frac{c'_{22}}{c'_{11}}}$	κ'	Roots	Cleavage System: Easy or Difficult
$YBa_2C_3O_{7-d}$ (Ortho-rhombic)	(001)[100]x[010]	0.764	0.8331	0.5784	Imaginary	Easy
MgO (FCC)	($\bar{1}$ 10)[001] x[110]	0.6513	1.0	0.6297	Imaginary	Easy

Table 40. Normalized elastic parameter, roots of characteristic equation, and the nature (easy or difficult) of the through-thickness cleavage system of the bicrystalline superlattice system 17.

Material (j) #	Cleavage System	A'	$\sqrt{\frac{c'_{22}}{c'_{11}}}$	κ'	Roots	Cleavage System: Easy or Difficult
$YBa_2C_3O_{7-d}$ (Ortho-rhombic)	(001)[100]x[010]	0.764	0.8331	0.5784	Imaginary	Easy
$SrTiO_3$ (Simple Cubic)	(010)[001]x[100]	3.6727	1.0	16.1473	Complex	Difficult

 doi:10.20944/preprints202403.1319.v1

Table 41. Normalized elastic parameter, roots of characteristic equation, and the nature (easy or difficult) of the through-thickness cleavage system of the bicrystalline superlattice system 18.

Material (j) #	Cleavage System	A'	$\sqrt{\frac{c'_{22}}{c'_{11}}}$	κ'	Roots	Cleavage System: Easy or Difficult
$YBa_2C_3O_{7-d}$ (Ortho-rhombic)	(001)[100]x[010]	0.764	0.8331	0.5784	Imaginary	Easy
$SrTiO_3$ (Simple Cubic)	$(\bar{1}10)$[001] x[110]	0.2723	1.0	0.3614	Imaginary	Easy

Table 42. Normalized elastic parameter, roots of characteristic equation, and the nature (easy or difficult) of the through-thickness cleavage system of the bicrystalline superlattice system 19.

Material (j) #	Cleavage System	A	$\sqrt{\frac{c'_{22}}{c'_{11}}}$	κ'	Roots	Cleavage System: Easy or Difficult
$YBa_2C_3O_{7-d}$ (Ortho-rhombic)	(010)[001]x[100]	0.8971	1.0771	0.9406	Imaginary	Easy
$SrTiO_3$ (Simple Cubic)	(010)[001]x[100]	3.6727	1.0	16.1473	Complex	Difficult

Table 46 summarizes the nature (easy or difficult) of the cleavage system in component phases of the afore-mentioned bicrystalline superlattice systems. It also lists the real or complex eigenvalues, $s = 0.5 \pm ie$, of these bicrystalline superlattices. These results suggest that the interfacial cracks would propagate in mixed (I/II) mode, primarily when both the component phases are characterized by difficult cleavage systems (complex roots), the exception being perovskite $SrTiO_3$ serving as the substrate (for $YBa_2C_3O_{7-d}$ or $YBa_2C_3O_7$ nano-films). A plausible reason for this exceptional behavior of $SrTiO_3$ may lie in its unusually high shear stiffness, c_{66}, which is substantially greater than its longitudinal stiffness, c_{11}, in combination with easiest cleavage system of $YBa_2C_3O_{7-d}$ (or $YBa_2C_3O_7$). This is in contrast with other cubic mono-crystals, such as FCC rock salt MgO. This fact results in negative Poisson's ratio effect, when rotated about the [001] axis by 45°, which is not generally encountered in cubic crystal elasticity. Additionally, this behavior is also in contrast with other easy cleavage systems of $YBa_2C_3O_{7-d}$ deposited on the same 45° rotated $SrTiO_3$, as shown in Tables 43, 45 and 46.

Table 43. Normalized elastic parameter, roots of characteristic equation, and the nature (easy or difficult) of the through-thickness cleavage system of the bicrystalline superlattice system 20.

Material (j) #	Cleavage System	A	$\sqrt{\frac{c'_{22}}{c'_{11}}}$	κ'	Roots	Cleavage System: Easy or Difficult
$YBa_2C_3O_{7-d}$ (Ortho-rhombic)	(010)[001]x[100]	0.8971	1.0771	0.9406	Imaginary	Easy
$SrTiO_3$ (Simple Cubic)	$(\bar{1}10)$[001] x[110]	0.2723	1.0	0.3614	Imaginary	Easy

 doi:10.20944/preprints202403.1319.v1

Table 44. Normalized elastic parameter, roots of characteristic equation, and the nature (easy or difficult) of the through-thickness cleavage system of the bicrystalline superlattice system 21.

Material (j) #	Cleavage System	A'	$\sqrt{\frac{c'_{22}}{c'_{11}}}$	κ'	Roots	Cleavage System: Easy or Difficult
$YBa_2C_3O_{7-d}$ (Ortho-rhombic)	$(\bar{1}00)[001]x[010]$	0.8971	0.9284	0.817	Imaginary	Easy
$SrTiO_3$ (Simple Cubic)	(010)[001]x[100]	3.6727	1.0	16.1473	Complex	Difficult

Table 45. Normalized elastic parameter, roots of characteristic equation, and the nature (easy or difficult) of the through-thickness cleavage system of the bicrystalline superlattice system 22 .

Material (j) #	Cleavage System	A'	$\sqrt{\frac{c'_{22}}{c'_{11}}}$	κ'	Roots	Cleavage System: Easy or Difficult
$YBa_2C_3O_{7-d}$ (Ortho-rhombic)	$(\bar{1}00)[001]x[010]$	0.8971	0.9284	0.817	Imaginary	Easy
$SrTiO_3$ (Simple Cubic)	$(\bar{1}10)[0\bar{1}01]$ x[110]	0.2723	1.0	0.3614	Imaginary	Easy

Table 46. Real or complex eigenvalues of the bicrystalline superlattice systems with through interfacial cracks.

Bicrystal System #	Nano-film/ Substrate	Cleavage Systems	Roots	Cleavage System: Easy or Difficult	s = 0.5 or s = 0.5±ie
1	Au/Si_3N_4	(010)[001]x[100]/ $(001)[0\bar{1}0]x[\bar{1}00]$	Complex/Imaginary	Difficult/Easy	0.5
2	Au/Si_3N_4	(010)[001]x[100]/ $(\bar{1}00)[0\bar{1}0]x[001]$	Complex/Imaginary	Difficult/Easy	0.5
3	Au/Si_3N_4	$(\bar{1}10)[001]x[110]$/ $(001)[00]x[\bar{1}00]$	Imaginary/Imaginary	Easy/Easy	0.5
4	Au/Si_3N_4	$(\bar{1}10)[001]x[110]$/ $(\bar{1}00)[0\bar{1}0]x[001]$	Imaginary/Imaginary	Easy/Easy	0.5
5	Au/MgO	(010)[001]x[100]/ (010)[001]x[100]	Complex/Complex	Difficult/Difficult	0.5±0.3814i 0.5±0.2108i
6	Au/MgO	(010)[001]x[100]/ (10)[001]x[110]	Complex/Imaginary	Difficult/Easy	0.5
7	Au/MgO	$(\bar{1}10)[001]x[110]$/ (010)[001]x[100]	Imaginary/Complex	Easy/Easy	0.5
8	Au/MgO	$(\bar{1}10)[001]x[110]$/ $(\bar{1}10)[001]x[110]$	Imaginary/Imaginary	Easy/Easy	0.5
9	$YBa_2C_3O_7$ $/Si_3N_4$	(010)[001]x[100]/ $(\bar{1}00)[0\bar{1}0]x[001]$	Complex/Imaginary	Difficult/Easy	0.5
10	$YBa_2C_3O_7$ $/SrTiO_3$	(010)[001]x[100]/ (010)[001]x[100]	Complex/Complex	Difficult/Difficult	0.5±0.7636i
11	$YBa_2C_3O_7$ $/SrTiO_3$	(010)[001]x[100]/	Complex/Imaginary	Difficult/Easy	0.5

 doi:10.20944/preprints202403.1319.v1

		($\bar{1}$ 10)[001]x[110]			
12	$YBa_2C_3O_7$ /$SrTiO_3$	($\bar{1}$ 10)[001]x[110]/ (010)[001]x[100]	Imaginary/Complex	Easy/Difficult	0.5
13	$YBa_2C_3O_7$ /$SrTiO_3$	($\bar{1}$ 10)[001]x[110]/ ($\bar{1}$ 10)[001]x[110]	Imaginary/Imaginary	Easy/Easy	0.5±0.0580i
14	$YBa_2C_3O_{7-d}$ /Si_3N_4	(001)[100]x[010]/ (001)[0 $\bar{1}$ 0]x[$\bar{1}$ 00]	Imaginary/Imaginary	Easy/Easy	0.5
15	$YBa_2C_3O_{7-d}$ /MgO	(001)[100]x[010]/ (010)[001]x[100]	Imaginary/Complex	Easy/Difficult	0.5
16	$YBa_2C_3O_{7-d}$ /MgO	(001)[100]x[010]/ ($\bar{1}$ 10)[001]x[110]	Imaginary/Imaginary	Easy/Easy	0.5
17	$YBa_2C_3O_{7-d}$ /$SrTiO_3$	(001)[100]x[010]/ (010)[001]x[100]	Imaginary/Complex	Easy/Difficult	0.5
18	$YBa_2C_3O_{7-d}$ /$SrTiO_3$	(001)[100]x[010]/ (10)[001]x[110]	Imaginary/Imaginary	Easy/Easy	0.5±0.1757i
19	$YBa_2C_3O_{7-d}$ /$SrTiO_3$	(010)[001]x[100]/ (010)[001]x[100]	Imaginary/Imaginary	Easy/Easy	0
20	$YBa_2C_3O_{7-d}$ /$SrTiO_3$	(010)[001]x[100]/ ($\bar{1}$ 10)[001]x[110]	Imaginary/Imaginary	Easy/Easy	0
21	$YBa_2C_3O_{7-d}$ /$SrTiO_3$	($\bar{1}$ 00)[001]x[010]/ (010)[001]x[100]	Imaginary/Imaginary	Easy/Easy	0
22	$YBa_2C_3O_{7-d}$ /$SrTiO_3$	($\bar{1}$ 00)[001]x[010]/ ($\bar{1}$ 10)[001]x[110]	Imaginary/Imaginary	Easy/Easy	0

$\bar{1}$.

9.2. Superlattice Trapping and Superlattice Crack Deflection (SCD)

The theory of lattice crack deflection (LCD) is discussed in Chaudhuri [49]. Table 47 displays the structures and elastic compliance constants of mono-crystalline FCC transition metal Au, FCC rock salt MgO, cubic perovskite $SrTiO_3$, HCP ceramic Si_3N_4, fully oxidized tetragonal $YBa_2C_3O_7$, and orthorhombic (superconducting) $YBa_2C_3O_{7-d}$ [49,59,78]. Table 48 shows the results for computed lattice crack deflection/deviation (LCD) parameters (energy barrier) and associated bond shear strains at crack deviation from a difficult cleavage system to an easy one, and their correlations with the anisotropic ratios relating to the difficult cleavage system along with Bravais lattice and structure. Only two crack systems are considered: {010}⟨001⟩x<100]> and $\{\bar{1}\,10\}$<001> x<110]>.

Table 47. Structures and elastic compliance constants of selected single crystals [49,78].

Single Crystal	Bravais Lattice	Structure	S_{11} (10^{-2} GPa^{-1})	S_{22} (10^{-2} GPa^{-1})	S_{33} (10^{-2} GPa^{-1})	S_{12} (10^{-2} GPa^{-1})	S_{13} (10^{-2} GPa^{-1})	S_{23} (10^{-2} GPa^{-1})	S_{44} (10^{-2} GPa^{-1})	S_{55} (10^{-2} GPa^{-1})	S_{66} (10^{-2} GPa^{-1})
Au [78,88]	FCC	FCC	2.355	2.355	2.355	-1.081	-1.081	-1.081	2.4096	2.4096	2.4096
MgO [78]	FCC	Rock Salt	0.4024	0.4024	0.4024	-0.0936	-0.0936	-0.0936	0.6461	0.6461	0.6461
$SrTiO_3$ [78]	Simple Cubic	Perovskite	0.33	0.33	0.33	-0.074	-0.074	-0.074	0.22	0.22	0.22
Si_3N_4	HCP	HCP	0.3576	0.3576	0.1852	-0.1255	-0.0464	-0.0464	0.8065	0.8065	0.9662
$YBa_2C_3O_7$	Tetra-gonal	Perovskite	0.6389	0.6389	1.1186	-0.1304	-0.339	-0.339	2.0	2.0	1.1765

 doi:10.20944/preprints202403.1319.v1

Y $Ba_2C_3O_{7-d}$	Ortho-rhombic	Perovskite	0.5003	0.4648	0.7054	-0.0678	-0.1564	-0.2115	2.0408	2.7027	1.2195

Table 48. Easy/difficult cleavage system, lattice crack deflection (LCD) barrier and associated bond shear strains in selected single crystals.

Crystal	Easy Cleavage System (ECS)	Difficult Cleavage System (DCS)	Aniso. Ratio, A, at DCS	Bond Shear Strain at Lattice Crack Deflection (γ_{bd})	Lattice Crack Deviation (LCD) Parameter in DCS (ΔK^*)
Au [88]	$\{\bar{1}10\}$<001> x<110]>	{010}⟨001⟩ x<110]>	2.8522	0.6438	0.8364
MgO	$\{\bar{1}10\}$<001> x<110]>	{010}⟨001⟩ x<100]>	1.5354	0.5353	0.6414
$SrTiO_3$	$\{\bar{1}10\}$<001> x<110]>	{010}⟨001⟩ x<100]>	3.6727	0.6075	0.5114
Si_3N_4	$(\bar{1}00)[0\bar{1}0]$ x[001]*	-------			
$YBa_2C_3O_7$	$\{\bar{1}10\}$<001> x<110]>	{010}⟨001⟩ x<100]>	1.9077	0.5055	0.6071
$YBa_2C_3O_{7-d}$	{001}<100> x<010>	-------			

For mono-crystalline FCC transition metals, {010}⟨001⟩x<100]> is deemed to be a difficult cleavage system for reasons explained above, while $\{\bar{1}10\}$<001>x<110]> is considered to be the preferred one for crack propagation. This is illustrated in Figure 26(a) of Chaudhuri [49]. Nonvanishing lattice crack deflection (LCD) energy barrier implies that a {010}⟨001⟩x<100]> through-crack in such single crystals would not deflect right at the appropriate Griffith/Irwin critical stress intensity factor (K_c) for mixed mode propagation because of the lattice effect, but would require additional bond shear strains for Au (Table 48). In the case of nonvanishing lattice crack deflection (LCD) barrier, e.g., in Au with moderately high anisotropic ratio, A = 2.8481 > 1, the difficult {010}⟨001⟩x<100]> crack may initially get lattice trapped and/or propagate in a "difficult" manner till an applied load somewhat higher than its Griffith mixed mode counterpart is reached, and then only deflect into the easy cleavage system, $\{\bar{1}10\}$<001>x<110]>. In addition, the bond breaking would not be continuous but abrupt. In contrast, for the same crystal with the very low modified anisotropic ratio, A' = 0.3494 < 1, lattice crack deflection (LCD) barrier vanishes and the easy $\{\bar{1}10\}$ <001>x<110]> crack would begin to propagate right at the Griffith/Irwin critical stress intensity factor. There would be no crack turning.

Bicrystals form superlattices, which has not been discussed, to the author's knowledge, in the anisotropic fracture mechanics literature [88]. However, the geometric mean of the two constituent phases would serve as a reasonably accurate procedure for computation of bond shear strain at superlattice crack deviation , γ_{bd}^{s}, and superlattice crack deflection (SCD) barrier, ΔK^{s*}; see also Chaudhuri [88]. A rigorous proof of this is currently being worked out, and will be presented in the near future. The numerical results are shown in Table 49. For a bicrystalline superlattice, e.g., Au/MgO (respectively, $YBa_2C_3O_7/SrTiO_3$), with both difficult cleavage systems, (010)[001]x[100]/(010)[001]x[100], serving as the interface, with the SCD barrier, ΔK^{s*}, value of 0.7324 (resp. 0.6240), the interfacial crack would encounter a tough interface, and would initially be superlattice-trapped and/or experience a mixed mode propagation in a "difficult" manner till an applied load somewhat higher than its Griffith/Irwin mixed mode interfacial fracture toughness

 doi:10.20944/preprints202403.1319.v1

counterpart –– quantified by ΔK^{s*} –– is reached, and thence deflect into the available easier cleavage system, $\{\bar{1}\,10\}$<001>x<110]>, of the component phase with the lower LCD barrier, ΔK^{*} = 0.6414 for MgO (resp. 0.5114 for $SrTiO_3$). In addition, the bond breaking would not be continuous but abrupt. In contrast, for the same bicrystalline superlattice, Au/MgO, with both easy ($\bar{1}$ 10)[001]x[110]/($\bar{1}$10)[001]x[110] cleavage systems serving as the interface, the SCD barrier, ΔK^{s*}, vanishes, and the easy interfacial crack would begin to propagate (in the absence of mode mixity) in a self-similar manner right at the Griffith/Irwin critical stress intensity factor. The bond breaking would be smooth and continuous. Interestingly, for the Au/MgO or $YBa_2C_3O_7/SrTiO_3$ superlattice, with one easy and the second one difficult, either (010)[001]x[100]/($\bar{1}$ 10)[001]x[110] or ($\bar{1}$ 10)[001]x[110]/(010)[001]x[100] cleavage systems serving as the interface, the SCD barrier, ΔK^{s*}, also vanishes, and the interfacial crack would begin to propagate (in the absence of mode mixity) on the easier side of and parallel to the interface at the Griffith/Irwin critical stress intensity factor. The bond breaking would be smooth and continuous on the easier side, but discontinuous and abrupt on the tougher side of the interface.

Table 49. Cleavage system, lattice crack deflection barrier and associated bond shear strains in selected bicrystalline superlattice systems.

Bicrystal System #	Nano-film/ Substrate	Cleavage Systems	Cleavage System: Easy or Difficult	Bond Shear Strain at Superlattice Crack Deflection $\left(\gamma_{bd}^{s}\right)$	Superlattice Crack Deviation (SCD) Parameter in DCS $\left(\Delta K^{s*}\right)$
1	Au/Si_3N_4	(010)[001]x[100]/ (001)[0$\bar{1}$0]x[$\bar{1}$00]	Difficult/Easy	0	0
2	Au/Si_3N_4	(010)[001]x[100]/ ($\bar{1}$00)[0$\bar{1}$0]x[001]	Difficult/Easy	0	0
3	Au/Si_3N_4	($\bar{1}$10)[001]x[110]/ (001)[0$\bar{1}$0]x[$\bar{1}$00]	Easy/Easy	0	0
4	Au/Si_3N_4	($\bar{1}$10)[001]x[110]/ ($\bar{1}$00)[0$\bar{1}$0]x[001]	Easy/Easy	0	0
5	Au/MgO	(010)[001]x[100]/ (010)[001]x[100]	Difficult/Difficult	0.4710	0.7324
6	Au/MgO	(010)[001]x[100]/ ($\bar{1}$10)[001]x[110]	Difficult/Easy	0	0
7	Au/MgO	($\bar{1}$10)[001]x[110]/ (010)[001]x[100]	Easy/Difficult	0	0
8	Au/MgO	($\bar{1}$10)[001]x[110]/ ($\bar{1}$10)[001]x[110]	Easy/Easy	0	0
9	$YBa_2C_3O_7$ /Si_3N_4	(010)[001]x[100]/ ($\bar{1}$00)[0$\bar{1}$0]x[001]	Difficult/Easy	0	0
10	$YBa_2C_3O_7$ /$SrTiO_3$	(010)[001]x[100]/ (010)[001]x[100]	Difficult/Difficult	0.5202	0.6240
11	$YBa_2C_3O_7$ /$SrTiO_3$	(010)[001]x[100]/ ($\bar{1}$10)[001]x[110]	Difficult/Easy	0	0
12	$YBa_2C_3O_7$ /$SrTiO_3$	($\bar{1}$10)[001]x[110]/ (010)[001]x[100]	Easy/Difficult	0	0
13	$YBa_2C_3O_7$ /$SrTiO_3$	($\bar{1}$10)[001]x[110]/ ($\bar{1}$10)[001]x[110]	Easy/Easy	0	0

 doi:10.20944/preprints202403.1319.v1

14	$YBa_2C_3O_{7-d}$ /Si3N4	(001)[100]x[010]/ (001)[0$\bar{1}$0]x[$\bar{1}$00]	Easy/Easy	0	0
15	$YBa_2C_3O_{7-d}$ /MgO	(001)[100]x[010]/ (010)[001]x[100]	Easy/Difficult	0	0
16	$YBa_2C_3O_{7-d}$ /MgO	(001)[100]x[010]/ ($\bar{1}$10)[001]x[110]	Easy/Easy	0	0
17	$YBa_2C_3O_{7-d}$ /SrTiO3	(001)[100]x[010]/ (010)[001]x[100]	Easy/Difficult	0	0
18	$YBa_2C_3O_{7-d}$ /SrTiO3	(001)[100]x[010]/ ($\bar{1}$10)[001]x[110]	Easy/Easy	0	0
19	$YBa_2C_3O_{7-d}$ /SrTiO3	(010)[001]x[100]/ (010)[001]x[100]	Easy/Difficult	0	0
20	$YBa_2C_3O_{7-d}$ /SrTiO3	(010)[001]x[100]/ ($\bar{1}$10)[001]x[110]	Easy/Easy	0	0
21	$YBa_2C_3O_{7-d}$ /SrTiO3	($\bar{1}$00)[001]x[010]/ (010)[001]x[100]	Easy/Difficult	0	0
22	$YBa_2C_3O_{7-d}$ /SrTiO3	($\bar{1}$00)[001]x[010]/ ($\bar{1}$10)[001]x[110]	Easy/Easy	0	0

For the Au/Si_3N_4 superlattice, with both easy cleavage systems, either ($\bar{1}$10)[001]x[110]/(001)[0$\bar{1}$0]x[$\bar{1}$00] or ($\bar{1}$10)[001]x[110]/($\bar{1}$00)[0$\bar{1}$0]x[001], serving as the interface, the SCD barrier, ΔK^{s*}, again vanishes, and the easy interfacial crack would begin to propagate (in the absence of mode mixity) in a self-similar manner right at the Griffith/Irwin critical stress intensity factor. The bond breaking would be smooth and continuous. As before, the same superlattice, with one easy and the second one difficult, either (010)[001]x[100]/(001)[0$\bar{1}$0]x[$\bar{1}$00] or (010)[001]x[100]/($\bar{1}$00)[0$\bar{1}$0]x[001] cleavage systems serving as the interface, ΔK^{s*} also vanishes, and the interfacial crack would begin to propagate (in the absence of mode mixity) on the easier side of and parallel to the interface at the Griffith/Irwin critical stress intensity factor. The bond breaking would be smooth and continuous on the easier side, but discontinuous and abrupt on the tougher side of the interface.

Similar situation prevails for $YBa_2C_3O_7/Si_3N_4$ superlattice, with one difficult and the second one easy, (010)[001]x[100]/($\bar{1}$00)[0$\bar{1}$0]x[001], serving as the interface.

For the orthorhombic perovskite/HCP $YBa_2C_3O_{7-d}/Si_3N_4$ superlattice, with both easy (001)[100]x[010]/(001)[0$\bar{1}$0]x[$\bar{1}$00] cleavage systems serving as the interface, the SCD barrier, ΔK^{s*}, again vanishes, and the easy interfacial crack would begin to propagate (in the absence of mode mixity) in a self-similar manner right at the Griffith/Irwin critical stress intensity factor. Similar results follow for the orthorhombic perovskite/FCC rock salt $YBa_2C_3O_{7-d}$/MgO superlattice, with both easy (001)[100]x[010]/($\bar{1}$10)[001]x[110] cleavage systems serving as the interface.

For the perovskite orthorhombic/FCC rock salt MgO bicrystalline superlattice, with both easy (001)[100]x[010]/($\bar{1}$10)[001]x[110] cleavage systems serving as the interface, ΔK^{s*} would again vanish, and the resulting easy interfacial crack would begin to propagate (in the absence of mode mixity) in a self-similar manner right at the Griffith/Irwin critical stress intensity factor. The bond breaking would be smooth and continuous. As before ΔK^{s*} for the same superlattice, with one easy and the second one difficult, (001)[100]x[010]/(010)[001]x[100] would also vanish, and the interfacial crack would begin to propagate (in the absence of mode mixity) on the easier side of and parallel to the interface at the Griffith/Irwin critical stress intensity factor. The bond breaking would be smooth and continuous on the easier side, but discontinuous and abrupt on the tougher side of the interface.

Finally, for the perovskite orthorhombic/cubic perovskite $YBa_2C_3O_{7-d}/SrTiO_3$ (respectively, $YBa_2C_3O_7/SrTiO_3$) bicrystalline superlattice, with both easy (001)[100]x[010]/($\bar{1}$10)[001]x[110] (resp., ($\bar{1}$10)[001]x[110]/($\bar{1}$10)[001]x[110]) cleavage systems serving as the interface, ΔK^{s*} would again

 doi:10.20944/preprints202403.1319.v1

vanish, and the resulting easy interfacial crack would experience a mixed mode propagation/growth right at the Griffith/Irwin critical complex stress intensity factor. Rice [9] has discussed the computation and interpretation of the resulting complex stress intensity factor (S.I.F.) for an isotropic bimaterial interface crack; see Sec. 9.3 below. The bond breaking is expected to be smooth and continuous. The reason for this exceptional behavior of $SrTiO_3$ lies, as has been explained above, in its unusually high shear stiffness, c_{66}, which is substantially greater than its longitudinal stiffness, c_{11}. However, ΔK^{s*} for the same superlattices, with one easy and the second one difficult, (001)[100]x[010]/(010)[001]x[100] for $YBa_2C_3O_{7-d}/SrTiO_3$, or $(\bar{1}10)$[001]x[110]/(010)[001]x[100] and (010)[001]x[100]/$(\bar{1}10)$[001]x[110] for $YBa_2C_3O_7/SrTiO_3$ also vanish, and the interfacial crack would begin to propagate (in the absence of mode mixity) on the easier side of and parallel to the interface at the Griffith/Irwin critical stress intensity factor. The bond breaking would be smooth and continuous on the easier side, but discontinuous and abrupt on the tougher side of the interface.

9.3. Complex Stress Intensity Factor (S.I.F.) and Raman Spectroscopic Surface Measurement

9.3.1. Complex Stress Intensity Factor (S.I.F.)

Rice [9] has discussed the validity of the complex stress intensity factor, $K = K_I + iK_{II}$, as a characterizing parameter in the context of a two-dimensional bi-material interface crack for material systems (of isotropic phases), for small scale yielding and small-scale contact zones at the crack tip. The proportion of opening and shearing modes at the interfacial crack tip is characterized by means of the phase angle, given by $\psi = \mathrm{Arctan}\left(K_{II} / K_I\right)$. Wang et al. [13] and Wu [90] have extended Rice's [9] analysis, and presented corresponding relations for interface cracks in monoclinic composites.

9.3.2. Raman Spectroscopic Surface Measurement of Carbon/Graphite Fiber-Epoxy Interfacial Bond

It has been argued by Chaudhuri et al. [36], in connection with Raman spectroscopic study of carbon-fiber epoxy interfacial debond, that in real-life composite materials, the fiber-matrix interface (a sharp material discontinuity) is replaced by an interphase region (of the order of 0.5 mm thickness), which permits us to ignore the contact of the Comninou [90] type (e = 0). Various factors that contribute to the formation of this interphase region are molecular entanglement following interdiffusion, electrostatic attraction, cationic groups at the ends of molecules attracted to an anionic surface that result in polymer matrix orientation at the fiber surface, chemical reaction, mechanical keying, etc. [91]. Additionally, the residual stress and coupling agents (e.g., silanes on glass fibers) applied to the fiber surface have pronounced effects on the interfacial bond strength. Under these circumstances, the macroscopic (mean field, e.g., linear elasticity) analysis presented above may be considered to be only a first approximation to the detailed microscopic (fluctuating) state of stress at the carbon fiber-epoxy debond tip. It may further be noted that the oscillatory behavior characterizing interpenetration of the component phases is not that unrealistic after all, but is rather a first-order approximation of the interdiffusion followed by molecular entanglement, chemical bonding and other similar microscopic (kinetic) phenomena studied by materials scientists.

A close scrutiny of two asymptotic solutions for bimaterials involving (i) the complex eigenvalues (e > 0), and (ii) their real counterpart (e = 0), in light of the Raman spectroscopic measurements, reveals that they represent two extreme cases of the interfacial (interphase) region of the carbon/graphite fibers with a polymeric matrix such as epoxy [36]. While the case (i) corresponds to an idealized carbon fiber with the surface layer(s) being comprised of completely disordered (amorphous) carbon resembling activated charcoal (R = I_{A1g} / I_{E2g} = 1), the case (ii) represents the idealized version of a graphite fiber with the surface layer(s) consisting of completely ordered (crystalline) carbon lattice resembling stress annealed pyrolite graphite (R = 0). Actual carbon/graphite fibers, both commercial and experimental, fall somewhere in between the two idealized extremes with 0 < R < 1. Therefore, the interfacial debond nucleation and propagation in an

 doi:10.20944/preprints202403.1319.v1

actual carbon/graphite fiber/epoxy matrix composite will be governed by solution with e replaced by [36]:

$$\bar{\varepsilon} = \varepsilon R = \varepsilon\left(I_{A1g} / I_{E2g}\right), \tag{36}$$

where I_{A1g} and I_{E2g} represent the relative (Raman) intensities of the peaks corresponding to the A_{1g} (weak) and E_{2g} (strong) modes, respectively. R represents the degree of chemical functionality (potential for strong or covalent bond formation). R ranges from 0.22 (Morganite I) to 0.85 (Thornel 10), with the industry standard AS4 being 0.811, as reported by Tuinstra and Koenig [92]. For the experimental fibers (grown in a carefully controlled environment to mimic their commercial counterparts) investigated by Chaudhuri et al. [36], R ranges from 0.279 to 0.785.

9.4. Through-thickness Distribution of Stress Intensity Factors (Fracture Toughness) and Energy Release Rates (Fracture Energy)

Figures 2a,b show variations of the normalized stress intensity factor, $K_{ij}^{*}(z) = K_{ij}(z) / K_{ij,\max)}$, i = I, II, III, j = 1, 2, through the thickness of a bicrystalline superlattice plate, weakened by through-crack investigated here. Figure 2a shows the through-thickness variation of the stress intensity factor for a far-field symmetrically distributed hyperbolic sine (mode I, II, III) load, while its antisymmetric counterpart, not encountered in two-dimensional analyses can be deemed associated with the singular residual stress field [89] and is displayed in Figure 2b. Figure 3 shows the corresponding variation of energy release rate, G^{*}, through the top half of the plate thickness. For through-thickness symmetric far-field loading, the crack is expected to grow through thickness in a stable manner till the stress intensity factor or the energy release rate reaches its critical value at the maximum location (just below the top and bottom surfaces). With further increase of the magnitude of the far-field loading, unstable crack growth is expected to progressively spread throughout the plate thickness. For skew-symmetric loading, as reported on earlier occasions [19], the bottom half will experience crack closure. Such types of results describing the three-dimensional distribution of stress intensity factors and energy release rates have only recently become available in the fracture mechanics literature.

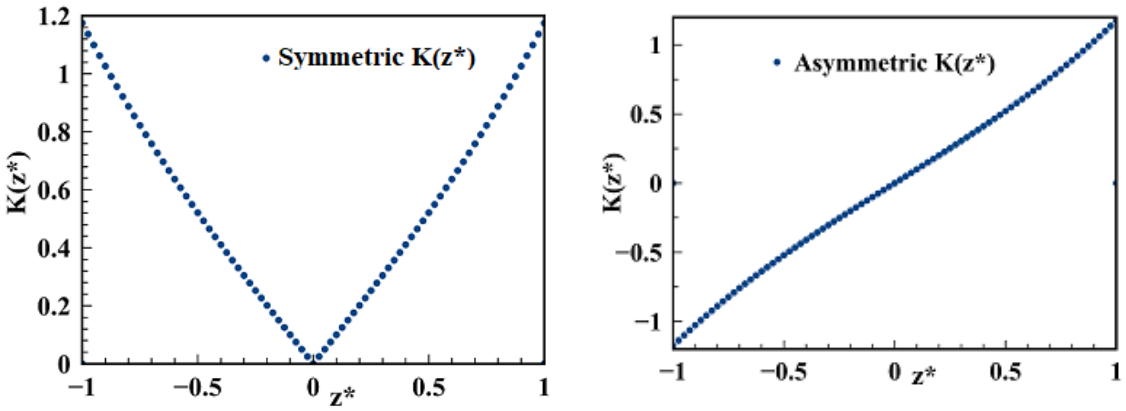

(**a**) (**b**)

Figure 2. Variation of stress intensity factors through thickness for sine hyperbolic load: (a) symmetric, (b) skew-symmetric.

 doi:10.20944/preprints202403.1319.v1

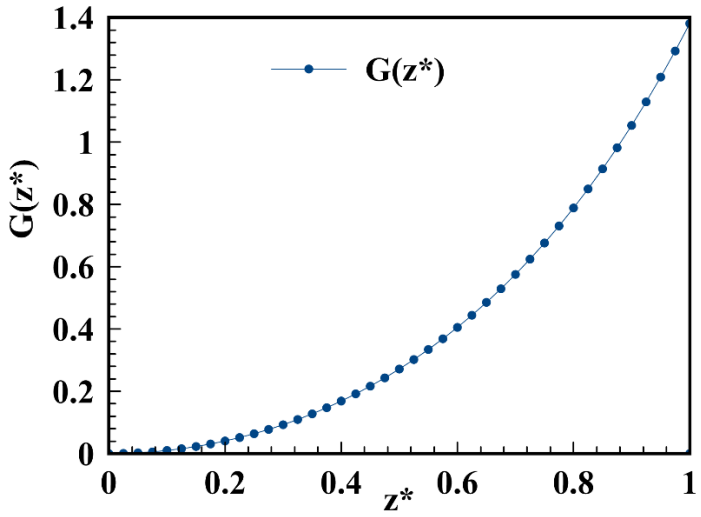

Figure 3. Variation of (mode I, II or III) energy release rate through thickness due to far-field sine hyperbolic load.

10. Summary and Conclusions

A recently developed eigenfunction expansion method, based in part on separation of the thickness-variable and partly utilizing a modified Frobenius type series expansion in terms of affine-transformed x-y coordinate variables of the Eshelby-Stroh type, is employed for obtaining three-dimensional asymptotic displacement and stress fields in the vicinity of the front of an interfacial crack weakening an infinite pie-shaped bicrystalline superlattice plate, of finite thickness, formed as a result of a mono-crystalline metal or superconductor film deposited over a substrate. The bicrystalline superlattice is made of orthorhombic (tetragonal, hexagonal and cubic as special cases) phases, and is subjected to the far-field extension/bending, in-plane shear/twisting and anti-plane shear loadings, distributed through the thickness. Crack-face boundary and interface contact conditions as well as those that are prescribed on the top and bottom surfaces of the bicrystalline superlattice plate are exactly satisfied.

It also extends a recently developed concept of lattice crack deflection (LCD) barrier to a superlattice, christened superlattice crack deflection (SCD) energy barrier for studying interfacial crack path instability, which can explain crack deflection from a difficult interface to an easier neighboring cleavage system. Additionally, the relationships of the nature (easy/easy, easy/difficult or difficult/difficult) interfacial cleavage systems based on the present solutions with the structural chemistry aspects of the component phases (such as orthorhombic, tetragonal, hexagonal as well as FCC (face centered cubic) transition metals and perovskites) of the superlattice are also investigated.

Important conclusions drawn from this study can be listed as follows:

(i) Atomistic scale modeling of interfacial cracks requires consideration of both the long-range elastic interactions and the short-range chemical reactions. The Griffith thermodynamic-based theory does not take the latter into account, and hence must be regarded as only a necessary condition (albeit being still very useful and widely employed) but not as sufficient.

(ii) The effect of short-range chemical reactions can be adequately captured by the elastic properties-based parameters, such as the planar anisotropic ratio, A_j, or equivalently, the normalized elastic parameter, k_j, j = 1, 2. This is because the elastic properties are controlled by various aspects of the underlying structural chemistry of single crystals, such as the Bravais lattice type, bonding (covalent, ionic, and metallic), bonding (including hybridized) orbitals, electro-negativity of constituent atoms in a compound, polarity, etc. More specifically, the elastic properties of superconducting $YBa_2Cu_3O_{7-d}$ are strongly influenced by oxygen non-stoichiometry (as well as various structural defects).

(iii) A single dimensionless parameters, such as the planar anisotropic ratio, A_j, or equivalently, the normalized elastic parameter, k_j, j = 1, 2, can serve as the Holy Grail quantity for an *a priori*

 doi:10.20944/preprints202403.1319.v1

determination of the status of a cleavage system to be easy or difficult, very much akin to Reynold's number for fluid flow problems, crossing a critical value of which signifies transition from one regime to another. Here, the planar anisotropic ratio, A_j, or equivalently, normalized elastic parameter, k_j, j = 1, 2, for a (010)[001]×[100] cleavage system, crossing the critical value of 1 or $\sqrt{c_{22}^{(j)} / c_{11}^{(j)}}$, j = 1, 2, respectively, signifies transitioning from self-similar crack growth or propagation to crack deflection or turning from a difficult cleavage system onto a nearby easy one. This is a significant qualitative as well as quantitative improvement over two-parameters based models, suggested by earlier researchers e.g. [13], in the context of two-dimensional anisotropic fracture mechanics.

(iv) Just as the introduction of Reynold's number facilitated design and setting up of experiments in addition to experimental verification of analytical and computational solutions in fluid dynamics, the accuracy and efficacy of the available test results on elastic constants of $YBa_2Cu_3O_{7-d}$ single crystals, measured by modern experimental techniques with resolutions at the atomic scale or nearly so, such as X-Ray diffraction, ultrasound technique, neutron diffraction/scattering, Brillouin spectroscopy/scattering, resonant ultrasound spectroscopy and the like is assessed with a powerful theoretical analysis on crack path stability/instability, in part based on a single dimensionless parameter, such as the planar anisotropic ratio, A_j, j = 1, 2.

(v) Experimental determination of surface energy, G_j, j = 1, 2, of the component phases or the corresponding interfacial energy, G_{int}, of a bicrystalline superlattice can sometimes be notoriously challenging, due to the presence of micro-to-nano scale defects, such as porosity, dislocation, twin boundaries, misalignment of bonds with respect to the loading axis, and the like. In contrast, the above-derived bond shear strain at superlattice crack deflection, γ_{bd}^{s}, and superlattice crack deflection (SCD) barrier, ΔK^{s*}, are, relatively speaking, much easier in comparison to determination of surface or interfacial energy.

(vi) Computed complex eigenvalues, s = 0.5±ie, for Au/MgO, and $YBa_2C_3O_7/SrTiO_3$, bicrystalline superlattices, with (010)[001]x[100]/(010)[001]x[100] serving as the interface suggest that the corresponding interfacial cracks would propagate in a mixed (I/II) mode. Likewise, for the bicrystalline superlattice, $YBa_2C_3O_{7-d}/SrTiO_3$ (resp. $YBa_2C_3O_7/SrTiO_3$) with (001)[100]x[010]/($\bar{1}$ 10)[001]x[110] (resp. ($\bar{1}$ 10)[001]x[110]/($\bar{1}$10)[001]x[110]) cleavage systems serving as the interface, the computed eigenvalues are also complex, resulting in a mixed (I/II) mode interfacial crack growth.

(vii) For the bicrystalline superlattice, Au/MgO (respectively, $YBa_2C_3O_7/SrTiO_3$), with both difficult cleavage systems, (010)[001]x[100]/(010)[001]x[100], serving as the interface, with the bond shear strain at superlattice crack deflection, γ_{bd}^{s}, value of 0.4710 (resp. 0.5202) and superlattice crack deflection (SCD) barrier ΔK^{s*}, value of 0.7324 (resp. 0.6240), the interfacial crack would encounter a tough interface, and would initially be superlattice-trapped and/or experience a mixed mode propagation in a "difficult" manner till an applied load somewhat higher than its Griffith/Irwin mixed mode interfacial fracture toughness counterpart –– quantified by ΔK^{s*} –– is reached, and thence deflect onto the available easier cleavage system, $\{\bar{1}\,10\}$<001>x<110]>, of the component phase with the lower LCD barrier, ΔK^{*} = 0.6414 for MgO (resp. 0.5114 for $SrTiO_3$). In addition, the bond breaking would not be continuous but abrupt.

(viii) In contrast, for the perovskite orthorhombic/cubic perovskite $YBa_2C_3O_{7-d}/SrTiO_3$ (respectively, $YBa_2C_3O_7/SrTiO_3$) bicrystalline superlattice, with both easy (001)[100]x[010]/($\bar{1}$ 10)[001]x[110] (resp., ($\bar{1}$10)[001]x[110]/($\bar{1}$10)[001]x[110]) cleavage systems serving as the interface, both bond shear strain at superlattice crack deflection, γ_{bd}^{s}, and superlattice crack deflection (SCD) barrier, ΔK^{s*}, vanish, and the resulting easy interfacial crack would experience a mixed mode propagation/growth right at the Griffith/Irwin-based critical complex stress intensity factor (S.I.F.), the computation and interpretation of which is expounded by Rice's [9] extension from a two-dimensional isotropic bimaterial interface crack to its to anisotropic counterpart. The bond breaking is expected to be smooth and continuous.

 doi:10.20944/preprints202403.1319.v1

(ix) For the Au/Si_3N_4 or $YBa_2C_3O_7$/Si_3N_4 superlattice, with both easy cleavage systems, either ($\bar{1}$10)[001]x[110]/(001)[0 $\bar{1}$ 0]x[$\bar{1}$00] or ($\bar{1}$10)[001]x[110]/($\bar{1}$00)[0$\bar{1}$0]x[001], serving as the interface, both bond shear strain at superlattice crack deflection, γ_{bd}^{s}, and superlattice crack deflection (SCD) barrier, ΔK^{s*}, vanish, and the easy interfacial crack would begin to propagate (in the absence of mode mixity) in a self-similar manner right at the Griffith/Irwin critical stress intensity factor. Likewise, a $YBa_2C_3O_{7-d}$/Si_3N_4 superlattice, with both easy cleavage systems, either {001}<100>x<010>/(001)[0 $\bar{1}$ 0]x[$\bar{1}$00] or {001}<100>x<010>/($\bar{1}$00)[0$\bar{1}$0]x[001], serving as the interface, would elicit a similar behavior. Other examples include Au/MgO (resp. $YBa_2C_3O_{7-d}$/MgO) bicrystalline superlattice with ($\bar{1}$10)[001]x[110/($\bar{1}$10)[001]x[110] (resp. {001}<100>x<010>/($\bar{1}$10)[001]x[110] cleavage systems serving as the interface. Similar response also ensues for the $YBa_2C_3O_{7-d}$/$SrTiO_3$ bicrystalline superlattice with (010)[001]x[100]/($\bar{1}$10)[001]x[110] or ($\bar{1}$00)[001]x[010]/($\bar{1}$10)[001]x[110] cleavage systems serving as the interface. The bond breaking would be smooth and continuous.

(x) Interestingly, for the Au/MgO or $YBa_2C_3O_7$/$SrTiO_3$ superlattice, with one easy and the second one difficult, either (010)[001]x[100]/($\bar{1}$10)[001]x[110] or ($\bar{1}$10)[001]x[110]/(010)[001]x[100] cleavage systems serving as the interface, the SCD barrier, ΔK^{s*}, also vanishes, and the interfacial crack would begin to propagate (in the absence of mode mixity) on the easier side of and parallel to the interface at the Griffith/Irwin critical stress intensity factor. Similar response ensues for the $YBa_2C_3O_{7-d}$/$SrTiO_3$ bicrystalline superlattice with {001}<100>x<010>/(010)[001]x[100] cleavage systems serving as the interface. Likewise, the Au/Si_3N_4 or $YBa_2C_3O_7$/Si_3N_4 superlattice with one easy and the second one difficult, either (010)[001]x[100]/(001)[0$\bar{1}$0]x[$\bar{1}$00] or (010)[001]x[100]/($\bar{1}$00)[0 $\bar{1}$ 0]x[001] cleavage systems serving as the interface, produces the same outcome. The bond breaking would be smooth and continuous on the easier side, but discontinuous and abrupt on the tougher side of the interface.

(xi) Finally, hitherto unavailable results, pertaining to the through-thickness variations of normalized stress intensity factors for symmetrically distributed hyperbolic sine load and its skew-symmetric counterpart that also satisfy the boundary conditions on the top and bottom surfaces of the bicrystalline superlattice plate, in the vicinity of an interfacial crack front, under investigation, bridge a longstanding gap in the interfacial stress singularity/fracture mechanics literature.

Appendix-A. Details of the Derivation of the Solution Involving Complex Roots for a (010)[001]×[100] Crack (Mode I/II Loading)

Some of the details of the mathematical derivation of the solution, involving complex roots, for an orthorhombic crystal plate, reinforced by (010) [001] through-anticrack and subjected to mode I/II loading (Section 4, Case (a)), are presented here. The components of displacement that satisfy the equilibrium equations (1) can be expressed in the following form:

$$u_j(r,\theta,z) = r^s D_{bj}(z)(ik)^s \Big[\Big\{(\cos(\theta)+\xi^{(j)}\sin(\theta))^2+\eta^{(j)^2}\sin^2(\theta)\Big\}^{s/2}\{A_{1_j}\cos(s\psi_j)+A_{2_j}\sin(s\psi_j)\}$$

$$+\ \{(\cos(\theta)-\xi^{(j)}\sin(\theta))^2\ +\ \eta^{(j)^2}\sin^2(\theta)\}^{s/2}\{A_{3_j}\cos(s\psi'_j)\ +\ A_{4_j}\sin(s\psi'_j)\}+O(r^{s+2}), \tag{A1a}$$

$$v_j(r,\theta,z) = r^s D_{bj}(z)(ik)^s \Big[\Big\{\cos^2(\theta)+\big(\xi'^{(j)}+\eta'^{(j)}\big)^2\sin^2(\theta)\Big\}^{s/2}\Big\{(H_{1j}A_{1j}+H_{2j}A_{2j})\cos(s\psi_j)$$

$$+(H_{1j}A_{2j}\ -\ H_{2j}A_{1j})\sin(s\psi_j)\}+\ \{(\cos(\theta)-\xi^{(j)}\sin(\theta))^2+\eta^{(j)^2}\sin^2(\theta)\}^{s/2}\{-(H_{1j}A_{3j}$$

$$+\ H_{2j}A_{4j})\cos(s\psi'_j)\ -(H_{1j}A_{4j}\ -\ H_{2j}A_{3j})\sin(s\psi'_j)\}+O(r^{s+2}), \tag{A1b}$$

$$w_j(r,\theta,z) = O(r^{s+2}), \tag{A1c}$$

and

 doi:10.20944/preprints202403.1319.v1

$$\sigma_{xj}(r,\theta,z) = r^{s-1}D_{bj}(z)\ (ik)^s s\ \langle\ \{(\cos(\theta)+\xi^{(j)}\sin(\theta))^2\ +\ \eta^{(j)^2}\sin^2(\theta)\}^{(s-1)/2}[(A_{1j}\{c_{11}^{(j)}$$
$$+(\xi^{(j)}H_{1j}-\eta^{(j)}H_{2j})c_{12}^{(j)}\}+A_{2j}\{(\eta^{(j)}H_{1j}+\xi^{(j)}H_{2j})c_{12}^{(j)}\})\cos((s-1)\psi_j)+(-A_{1j}\{(\eta^{(j)}H_{1j}+\xi^{(j)}H_{2j})c_{12}^{(j)}\}$$
$$+A_{2j}\{c_{11}^{(j)}+(\xi^{(j)}H_{1j}-\eta^{(j)}H_{2j})c_{12}^{(j)}\})\sin((s-1)\psi_j)]+\ \{(\cos(\theta)-\xi^{(j)}\sin(\theta))^2$$
$$+\eta^{(j)^2}\sin^2(\theta)\}^{(s-1)/2}[(A_{3j}\{c_{11}^{(j)}+(\xi^{(j)}H_{1j}-\eta^{(j)}H_{2j})c_{12}^{(j)}\}+A_{4j}\{(\eta^{(j)}H_{1j}+\xi^{(j)}H_{2j})c_{12}^{(j)}\})\cos((s-1)\psi'_j)$$
$$+(-A_{3j}\{(\eta^{(j)}H_{1j}+\xi^{(j)}H_{2j})c_{12}^{(j)}\}\ +A_{4j}\{c_{11}^{(j)}+(\xi^{(j)}H_{1j}-\eta^{(j)}H_{2j})c_{12}^{(j)}\})\sin((s-1)\psi'_j)]\ \rangle \qquad \text{(A2a)}$$

$$\sigma_{yj}(r,\theta,z) = r^{s-1}D_{bj}(z)\ (ik)^s s\ \langle\ \{(\cos(\theta)+\xi^{(j)}\sin(\theta))^2+\eta^{(j)^2}\sin^2(\theta)\}^{(s-1)/2}[(A_{1j}\{c_{12}^{(j)}$$
$$+(\xi^{(j)}H_{1j}-\eta^{(j)}H_{2j})c_{22}^{(j)}\}+A_{2j}\{(\eta^{(j)}H_{1j}+\xi^{(j)}H_{2j})c_{22}^{(j)}\})\cos((s-1)\psi_j)+(-A_{1j}\{(\eta^{(j)}H_{1j}+\xi^{(j)}H_{2j})c_{22}^{(j)}\}$$
$$+A_{2j}\{c_{12}^{(j)}+(\xi^{(j)}H_{1j}-\eta^{(j)}H_{2j})c_{22}^{(j)}\})\sin((s-1)\psi_j)]+\ \{(\cos(\theta)-\xi^{(j)}\sin(\theta))^2$$
$$+\eta^2\sin^2(\theta)\}^{(s-1)/2}[(A_{3j}\{c_{12}^{(j)}+(\xi^{(j)}H_{1j}-\eta^{(j)}H_{2j})c_{22}^{(j)}\}+A_{4j}\{(\eta^{(j)}H_{1j}+\xi^{(j)}H_{2j})c_{22}^{(j)}\})\cos((s-1)\psi'_j)$$
$$+(-A_{3j}\{(\eta^{(j)}H_{1j}+\xi^{(j)}H_{2j})c_{22}^{(j)}\}+A_{4j}\{c_{12}^{(j)}+(\xi^{(j)}H_{1j}-\eta^{(j)}H_{2j})c_{22}^{(j)}\})\sin((s-1)\psi'_j)]\rangle \qquad \text{(A2b)}$$

$$\tau_{xyj}(r,\theta,z) = r^{s-1}D_{b1}(z)(ik)^s s\ c_{66}^{(j)}\Big\langle\{(\cos(\theta)+\xi^{(j)}\sin(\theta))^2+\eta^{(j)^2}\sin^2(\theta)\}^{(s-1)/2}[\{A_{1j}(\xi^{(j)}+H_{1j})$$
$$+A_{2j}(\eta^{(j)}+H_{2j})\}\cos((s-1)\psi_j)+\{-A_{1j}(\eta^{(j)}+H_{2j})+A_{2j}(\xi^{(j)}+H_{1j})\}\sin((s-1)\psi_j)]$$
$$+\{(\cos(\theta)-\xi^{(j)}\sin(\theta))^2+\eta^{(j)^2}\sin^2(\theta)\}^{(s-1)/2}[\{-A_{3j}(\xi^{(j)}+H_{1j})-A_{4j}(\eta^{(j)}+H_{2j})\}\cos((s-1)\psi'_j)$$
$$+\{A_{3j}(\eta^{(j)}+H_{2j})-A_{4j}(\xi^{(j)}+H_{1j})\}\sin((s-1)\psi'_j)]\ \rangle+\ O(r^{s+1}), \qquad \text{(A2c)}$$

$$\sigma_{zj}(r,\theta,z) = r^{s-1}D_{bj}(z)\ (ik)^s s\ \langle\ \{(\cos(\theta)+\xi^{(j)}\sin(\theta))^2\ +\ \eta^{(j)^2}\sin^2(\theta)\}^{(s-1)/2}[(A_{1j}\{c_{12}^{(j)}$$
$$+(\xi^{(j)}H_{1j}-\eta^{(j)}H_{2j})c_{23}^{(j)}\}+A_{2j}\{(\eta^{(j)}H_{1j}+\xi^{(j)}H_{2j})c_{23}^{(j)}\})\cos((s-1)\psi_j)+(-A_{1j}\{(\eta^{(j)}H_{1j}+\xi^{(j)}H_{2j})c_{23}^{(j)}\}$$
$$+A_{2j}\{c_{12}^{(j)}+(\xi^{(j)}H_{1j}-\eta^{(j)}H_{2j})c_{23}^{(j)}\})\sin((s-1)\psi_j)]+\ \{(\cos(\theta)-\xi^{(j)}\sin(\theta))^2$$
$$+\eta^{(j)^2}\sin^2(\theta)\}^{(s-1)/2}[(A_{3j}\{c_{12}^{(j)}+(\xi^{(j)}H_{1j}-\eta^{(j)}H_{2j})c_{23}^{(j)}\}+A_{4j}\{(\eta^{(j)}H_{1j}+\xi^{(j)}H_{2j})c_{23}^{(j)}\})\cos((s-1)\psi'_j)$$
$$+(-A_{3j}\{(\eta^{(j)}H_{1j}+\xi^{(j)}H_{2j})c_{23}\}+A_{4j}\{c_{13}^{(j)}+(\xi^{(j)}H_{1j}-\eta^{(j)}H_{2j})c_{23}^{(j)}\})\sin((s-1)\psi'_j)]\rangle \qquad \text{(A2d)}$$

$$\tau_{xzj}(r,\theta,z) = O(r^s), \qquad \tau_{yzj}(r,\theta,z) = O(r^s). \qquad \text{(A2e,f)}$$

in which s = 1 – l, l being the strength or order of the stress singularity, and

$$D_{bj}(z) = D_{1j}\sin(\alpha z)+D_{2j}\cos(\alpha z), \qquad j=1,2 \qquad \text{(A3)}$$

$$H_{1j} = -\frac{\xi^{(j)}\ (\sqrt{c_{11}^{(j)}\ c_{22}^{(j)}}+\ c_{66}^{(j)})}{(c_{12}^{(j)}\ +\ c_{66}^{(j)})}, \qquad H_{2j} = \frac{\eta^{(j)}\ (\sqrt{c_{11}^{(j)}\ c_{22}^{(j)}}-\ c_{66}^{(j)})}{(c_{12}^{(j)}\ +\ c_{66}^{(j)})}. \qquad \text{(A4a,b)}$$

$$\cos(\psi_j(\theta)) = \frac{\cos(\theta)+\xi^{(j)}\sin(\theta)}{\{(\cos(\theta)+\xi^{(j)}\sin(\theta))^2\ +\ \eta^{(j)^2}\sin^2(\theta)\}^{1/2}}, \qquad \text{(A5a)}$$

$$\sin(\psi_j(\theta)) = \frac{\eta^{(j)}\sin(\theta)}{\{(\cos(\theta)+\xi^{(j)}\sin(\theta))^2\ +\ \eta^{(j)^2}\sin^2(\theta)\}^{1/2}}, \qquad \text{(A5b)}$$

$$\cos(\psi'_j(\theta)) = \frac{\cos(\theta)-\xi^{(j)}\sin(\theta)}{\{(\cos(\theta)-\xi^{(j)}\sin(\theta))^2\ +\ \eta^{(j)^2}\sin^2(\theta)\}^{1/2}}, \qquad \text{(A5c)}$$

$$\sin(\psi'(\bar{\theta})) = \frac{-\eta\sin(\bar{\theta})}{\{(\cos(\bar{\theta})-\xi\sin(\bar{\theta}))^2\ +\ \eta^2\sin^2(\bar{\theta})\}^{1/2}}, \qquad \text{(A5d)}$$

A_{ij} , i = 1,...,4, j = 1, 2, are undetermined coefficients (i.e., eigenvectors related to "stress intensity factors"). It may be noted that since s or Re s (when s is complex) is positive, all the higher order terms in Eqs. (A2) vanish as r ® 0. The components of displacement can now be expressed in the cylindrical polar coordinate system as follows:

 doi:10.20944/preprints202403.1319.v1

$$u_{rj}(r,\theta,z) = r^s D_{bj}(z)\,(ik)^s \left\langle \left\{\left(\cos(\theta)+\xi^{(j)}\sin(\theta)\right)^2 + \eta^{(j)2}\sin^2(\theta)\right\}^{s/2}\left[\left\{A_{1j}\cos(\theta)+ \left(H_{1j}A_{1j}+H_{2j}A_{2j}\right)\sin(\theta)\right\}\cos\left(s\psi_j\right) + \left\{A_{2j}\cos(\theta)+\left(H_{1j}A_{2j}-H_{2j}A_{1j}\right)\sin(\theta)\right\}\sin\left(s\psi_j\right)\right] + \left\{\left(\cos(\theta)-\xi^{(j)}\sin(\theta)\right)^2+\eta^{(j)2}\sin^2(\theta)\right\}^{s/2}\left[\left\{A_{3j}\cos(\theta)+\left(-H_{1j}A_{3j}+H_{2j}A_{4j}\right)\sin(\theta)\right\}\cos\left(s\psi'_j\right) + \left\{A_{4j}\cos(\theta)-\left(H_{1j}A_{4j}-H_{2j}A_{3j}\right)\sin(\theta)\right\}\sin\left(s\psi'_j\right)\right]\right\rangle + O\left(r^{s+2}\right), \tag{A6a}$$

$$u_{\theta j}(r,\theta,z) = r^s D_{bj}(z)\,(ik)^s \left\langle \left\{\left(\cos(\theta)+\xi^{(j)}\sin(\theta)\right)^2 + \eta^{(j)2}\sin^2(\theta)\right\}^{s/2}\left[\left\{-A_{1j}\sin(\theta)+ \left(H_{1j}A_{1j}+H_{2j}A_{2j}\right)\cos(\theta)\right\}\cos\left(s\psi_j\right) + \left\{-A_{2j}\sin(\theta)+\left(H_{1j}A_{2j}-H_{2j}A_{1j}\right)\cos(\theta)\right\}\sin\left(s\psi_j\right)\right] + \left\{\left(\cos(\theta)-\xi^{(j)}\sin(\theta)\right)^2+\eta^{(j)2}\sin^2(\theta)\right\}^{s/2}\left[-\left\{A_{3j}\sin(\theta)+\left(H_{1j}A_{3j}- H_{2j}A_{4j}\right)\cos(\theta)\right\}\cos\left(s\psi'_j\right) - \left\{A_{4j}\sin(\theta)+\left(H_{1j}A_{4j}+H_{2j}A_{3j}\right)\cos(\theta)\right\}\sin\left(s\psi'_j\right)\right] + O\left(r^{s+2}\right), \tag{A6b}$$

$$w_j(r,\theta,z) = O\left(r^{s+1}\right). \tag{A6c}$$

Similarly, the components of the asymptotic stress field can be conveniently expressed by using standard transformation rule:

$$\begin{Bmatrix}\sigma_{rj}\\ \sigma_{\theta j}\\ \tau_{r\theta j}\end{Bmatrix} = \begin{bmatrix}\cos^2(\theta) & \sin^2(\theta) & \sin(2\theta)\\ \sin^2(\theta) & \cos^2(\theta) & -\sin(2\theta)\\ -\frac{1}{2}\sin(2\theta) & \frac{1}{2}\sin(2\theta) & \cos(2\theta)\end{bmatrix}\begin{Bmatrix}\sigma_{xj}\\ \sigma_{yj}\\ \tau_{xyj}\end{Bmatrix}, \tag{A7a}$$

$$\begin{Bmatrix}\tau_{rzj}\\ \tau_{\theta zj}\end{Bmatrix} = \begin{bmatrix}\cos(\theta) & \sin(\theta)\\ -\sin(\theta) & \cos(\theta)\end{bmatrix}\begin{Bmatrix}\tau_{xzj}\\ \tau_{yzj}\end{Bmatrix}. \tag{A7b}$$

The stress component, s_{zj}, is as given in (A2d).

Appendix-B: Details of the Derivation of the Solution Involving Imaginary Roots for a (010)[001]×[100] Crack (Mode I/II Loading)

This appendix provides some of the details of the mathematical derivation of the solution, involving imaginary roots, for an orthorhombic crystal plate, weakened by (010) [001] through-crack and subjected to mode I/II loading (Section 4, Case (b)). The components of displacement that satisfy the equilibrium equations (1) can be expressed in the following form:

$$u_j(r,\theta,z) = r^s D_{bj}(z)(ik)^s\left[\left\{\cos^2(\theta)+\left(\xi'^{(j)}+\eta'^{(j)}\right)^2\sin^2(\theta)\right\}^{s/2}\left\{A_{1j}\cos\left(s\psi_{1j}\right)+A_{2j}\sin\left(s\psi_{1j}\right)\right\} + \left\{\cos^2(\bar{\theta})+\left(\xi'^{(j)}-\eta'^{(j)}\right)^2\sin^2(\theta)\right\}^{s/2}\left\{A_{3j}\cos\left(s\psi'_{1j}\right)+A_{4j}\sin\left(s\psi'_{1j}\right)\right\}\right]+O\left(r^{s+2}\right), \tag{B1a}$$

$$v_j(r,\theta,z) = r^s D_{bj}(z)(ik)^s\left[\left\{\cos^2(\theta)+\left(\xi'^{(j)}+\eta'^{(j)}\right)^2\sin^2(\theta)\right\}^{s/2}\left\{-H'_{1j}A_{2j}\cos\left(s\psi_{1j}\right)+H'_{1j}A_{1j}\sin\left(s\psi_{1j}\right)\right\} + \left\{\cos^2(\theta)+\left(\xi'^{(j)}-\eta'^{(j)}\right)^2\sin^2(\theta)\right\}^{s/2}\left\{-H'_{2j}A_{41}\cos\left(s\psi'_{1j}\right)+H'_{2j}A_{3j}\sin\left(s\psi'_{1j}\right)\right\}\right]+O\left(r^{s+2}\right), \tag{B1b}$$

$$w_j(r,\theta,z) = O\left(r^{s+1}\right). \tag{B1c}$$

and

$$\sigma_{xj}(r,\theta,z) = r^{s-1}D_{bj}(z)\,(ik)^s s\left\langle\left\{\cos^2(\theta)+\left(\xi'^{(j)}+\eta'^{(j)}\right)^2\sin^2(\theta)\right\}^{(s-1)/2}\left\{c_{11}^{(j)}+ H'_{1j}\left(\xi'+\eta'\right)c_{12}^{(j)}\right\}\left\{A_{1j}\cos\left((s-1)\psi_{1j}\right)+A_{2j}\sin\left((s-1)\psi_{1j}\right)\right\}+\left\{\cos^2(\theta)+ \left(\xi'^{(j)}-\eta'^{(j)}\right)^2\sin^2(\theta)\right\}^{(s-1)/2}\left\{c_{11}^{(j)}+H'_{2j}\left(\xi'^{(j)}-\eta'^{(j)}\right)c_{12}^{(j)}\right\}\left\{A_{3j}\cos\left((s-1)\psi'_{1j}\right)+A_{4j}\sin\left((s-1)\psi'_{1j}\right)\right\}\right\rangle \tag{B2a}$$

 doi:10.20944/preprints202403.1319.v1

$$\sigma_{yj}(r,\theta,z) = r^{s-1}D_{bj}(z)\ (ik)^s s \Big\langle \{\cos^2(\theta)+(\xi'+\eta')^2\sin^2(\theta)\}^{(s-1)/2}\{c_{12}^{(j)} + H'_{1j}(\xi'^{(j)}+\eta'^{(j)})c_{22}^{(j)}\}\{A_{1j}\cos((s-1)\psi_{1j})+A_{2j}\sin((s-1)\psi_{1j})\}+\{\cos^2(\theta)+(\xi'^{(j)}-\eta'^{(j)})^2\sin^2(\theta)\}^{(s-1)/2}\{c_{12}^{(j)}+H'_{2j}(\xi'^{(j)}-\eta'^{(j)})c_{22}^{(j)}\}\{A_{3j}\cos((s-1)\psi'_{1j})+A_{4j}\sin((s-1)\psi'_{1j})\}\Big\rangle \quad \text{(B2b)}$$

$$\tau_{xyj}(r,\theta,z) = r^{s-1}D_{bj}(z)(ik)^s s\ c_{66}^{(j)}\Big\langle \{\cos^2(\theta)+(\xi'^{(j)}+\eta'^{(j)})^2\sin^2(\theta)\}^{(s-1)/2}\{H'_{1j} - (\xi'^{(j)}+\eta'^{(j)})\}\{-A_{2j}\cos((s-1)\psi_{1j})+A_{1j}\sin((s-1)\psi_{1j})\} + \{\cos^2(\theta)+(\xi'^{(j)}-\eta'^{(j)})^2\sin^2(\theta)\}^{(s-1)/2}\{H'_{2j}-(\xi'^{(j)}-\eta'^{(j)})\}\{-A_{4j}\cos((s-1)\psi_{1j})+A_{3j}\sin((s-1)\psi_{1j})\}\Big\rangle \quad \text{(B2c)}$$

$$\sigma_{zj}(r,\theta,z) = r^{s-1}D_{bj}(z)\ (ik)^s s \Big\langle \{\cos^2(\theta)+(\xi'^{(j)}+\eta'^{(j)})^2\sin^2(\theta)\}^{(s-1)/2}\{c_{12}^{(j)} + H'_{1j}(\xi'^{(j)}+\eta'^{(j)})c_{23}^{(j)}\}\{A_{1j}\cos((s-1)\psi_{1j})+A_{2j}\sin((s-1)\psi_{1j})\}+\{\cos^2(\theta)+(\xi'^{(j)}-\eta'^{(j)})^2\sin^2(\theta)\}^{(s-1)/2}\{c_{12}^{(j)}+H'_{2j}(\xi'^{(j)}-\eta'^{(j)})c_{23}^{(j)}\}\{A_{3j}\cos((s-1)\psi'_{1j})+A_{4j}\sin((s-1)\psi'_{1j})\}\Big\rangle \quad \text{(B2d)}$$

$$\tau_{xzj}(r,\theta,z) = O(r^s), \qquad \tau_{yzj}(r,\theta,z) = O(r^s). \quad \text{(B2e,f)}$$

in which

$$H'_{1j} = -\frac{\{\sqrt{c_{11}^{(j)}c_{22}^{(j)}} - c_{66}^{(j)}(\xi'^{(j)}+\eta'^{(j)})^2\}}{(c_{12}^{(j)}+c_{66}^{(j)})(\xi'^{(j)}+\eta'^{(j)})}, \qquad H'_{2j} = \frac{\{\sqrt{c_{11}^{(j)}c_{22}^{(j)}} - c_{66}^{(j)}(\xi'^{(j)}-\eta'^{(j)})^2\}}{(c_{12}^{(j)}+c_{66}^{(j)})(\xi'^{(j)}-\eta'^{(j)})}. \quad \text{(B3a,b)}$$

and

$$\cos(\psi_{1j}(\theta)) = \frac{\cos(\theta)}{\{\cos^2(\theta)+(\xi'^{(j)}+\eta'^{(j)})^2\sin^2(\theta)\}^{1/2}}, \quad \text{(B4a)}$$

$$\sin(\psi_{1j}(\theta)) = \frac{(\xi'^{(j)}+\eta'^{(j)})\sin(\theta)}{\{\cos^2(\theta)+(\xi'^{(j)}+\eta'^{(j)})^2\sin^2(\theta)\}^{1/2}}, \quad \text{(B4b)}$$

$$\cos(\psi'_{1j}(\theta)) = \frac{\cos(\theta)}{\{\cos^2(\theta)+(\xi'^{(j)}-\eta'^{(j)})^2\sin^2(\theta)\}^{1/2}}, \quad \text{(B4c)}$$

$$\sin(\psi'_{1j}(\theta)) = \frac{(\xi'^{(j)}-\eta'^{(j)})\sin(\theta)}{\{\cos^2(\theta)+(\xi'^{(j)}-\eta'^{(j)})^2\sin^2(\theta)\}^{1/2}}, \quad \text{(B4d)}$$

It may be noted that since s or Re s (when s is complex) is positive, all the higher order terms in Eqs. (B2) vanish as r ® 0. The components of displacement can now be expressed in the cylindrical polar coordinate system as follows:

$$u_{rj}(r,\theta,z) = r^s D_{bj}(z)(ik)^s\Big\langle \{\cos^2(\theta)+(\xi'^{(j)}+\eta'^{(j)})^2\sin^2(\theta)\}^{s/2}\Big[\{A_{1j}\cos(\theta)-H'_{1j}A_{2j}\sin(\theta)\}\cos(s\psi_{1j})$$
$$+\{A_{2j}\cos(\theta)+H'_{1j}A_{1j}\sin(\theta)\}\sin(s\psi_{1j})\Big]+\{\cos^2(\theta)+(\xi'^{(j)}-\eta'^{(j)})^2\sin^2(\theta)\}^{s/2}\Big[\{A_{3j}\cos(\theta)$$
$$-H'_{2j}A_{4j}\sin(\theta)\}\cos(s\psi'_{1j})+\{A_{4j}\cos(\theta)+H'_{2j}A_{3j}\sin(\theta)\}\sin(s\psi'_{1j})\Big]\Big\rangle + O(r^{s+2}), \quad \text{(B5a)}$$

$$u_{\theta j}(r,\theta,z) = r^s D_{bj}(z)(ik)^s\Big\langle \{\cos^2(\theta)+(\xi'^{(j)}+\eta'^{(j)})^2\sin^2(\theta)\}^{s/2}\Big[-\{A_{1j}\sin(\theta)+H'_{1j}A_{2j}\cos(\theta)\}\cos(s\psi_{1j})$$
$$+\{-A_{2j}\sin(\theta)+H'_{1j}A_{1j}\cos(\theta)\}\sin(s\psi_{1j})\Big]+\{\cos^2(\theta)+(\xi'^{(j)}-\eta'^{(j)})^2\sin^2(\theta)\}^{s/2}\Big[-\{A_{3j}\sin(\theta)$$
$$+H'_{2j}A_{4j}\cos(\theta)\}\cos(s\psi'_{1j})+\{-A_{4j}\sin(\theta)+H'_{2j}A_{3j}\cos(\theta)\}\Big\rangle + O(r^{s+2}), \quad \text{(B5b)}$$

$$w_j(r,\theta,z) = O(r^{s+1}). \quad \text{(B5c)}$$

Similarly, the components of the asymptotic stress field can be conveniently expressed by using standard transformation rule, given earlier in eqn. (A7). The stress component, s_Z, is as given in eqn. (B2d).

References

1. Chaudhuri RA. Three-dimensional singular stress fields near the circumferential junction corner line of an island/substrate system either free-standing or fully/partially bonded to a rigid block. Eng. Fracture Mech. 2013; 107: 80-97. Doi: 10.1016/j.engfracmech.2013.02.012
2. Lin XM, Jaeger HM, Sorensen CM, Klabunde KJ. Formation of long-range-ordered nanocrystal superlattices on silicon nitride substrates. J. Phys. Chem. B, 2001; 105: 3353–3357.
3. Ovsyannikov GA, Borisenko IV, Constantinian KY, Kislinski YV, Hakhoumian A, Pogosyan NG, Zakaryan TV. Josephson bicrystal junctions on sapphire substrates for THz frequency application. J. Superconductivity and Novel Magnetism 2006; 19: 669-673.
4. Pashley DW, Stowell MJ, Jacobs MH, Law TJ. The growth and structure of gold and silver deposits formed by evaporation inside an electron microscope. Philosoph. Magazine 1964; 10: 127-158.
5. Yin E., Rubin MD, Dixon MA. Sputtered YBCO Films on Metal Substrates. J. Mater. Res. 1992; 7(7): 1636–1640. Doi: 10.1557/JMR.1992.1636
6. Lekhnitskii SG. Anisotropic Plates. Gordon and Breach, New York (1968).
7. Stroh AN. Dislocations and cracks in anisotropic elasticity. Phil. Magazine 1958; 7: 625-646. Doi: 10.1080/14786435808565804
8. Nazarov SA. Stress intensity factors and crack deviation conditions in a brittle anisotropic solid. J. Appl. Mech. Techn. Phys. 2005; 36: 386-394.
9. Rice JR. Elastic fracture mechanics concepts for interfacial cracks. ASME J. Appl. Mech. 1988; 55: 98-103.
10. Wu K-C. Stress intensity factors and energy release rate for interfacial cracks between dissimilar anisotropic materials. ASME J. Appl. Mech. 1990; 57: 882-886.
11. Chaudhuri RA, Xie M, Garala HJ. Stress singularity due to kink band weakening a unidirectional composite under compression. J. Compos. Materials 1996; 30(6): 672-691. Doi: 10.1177/002199839603000603
12. Qu J, Bassani JL. Cracks on bimaterial and bicrystal interfaces. J. Mech. Phys. Solids. 1989; 37: 417-433.
13. Wang, T.-C. W., Shih, C. F., & Suo, Z. (1992). Crack extension and kinking in laminates and bicrystals. *International Journal of Solids and Structures*, 29: 327-344.
14. Suo Z, Bao G, Fan B, Wang TC. Orthotropy rescaling and implications for fracture in composites. Int. J. Solids Struct. 1991; 28(2): 235-248. D
15. Lin YY, Sung JC. Stress singularities at the apex of a dissimilar anisotropic wedge. ASME J. Appl. Mech.1998; 65: 454-463. Doi: 10.1115/1.2789075
16. Stenger F, Chaudhuri R, Chiu J. Sinc solution of boundary integral form for two-dimensional bi-material elasticity problems. Compos. Sci. Tech. 2000; 60(12-13): 2197–2211. Doi: 10.1016/S0266-3538(00)00015-4
17. Dal Corso F, Bigoni D. The interactions between shear bands and rigid lamellar inclusions in a ductile metal matrix. Proc. Royal Soc. A, 2009, 465, 143-163.
18. Chaudhuri RA, Xie M. A novel eigenfunction expansion solution for three-dimensional crack problems. Compos. Sci. Tech. 2000; 60(12-13): 2565-2580. Doi: 10.1016/S0266-3538(00)00050-6
19. Chaudhuri RA. On through-thickness distribution of stress intensity factors and energy release rates in the vicinity of crack fronts. Eng. Fracture Mech. 2019; 216: 106478. Doi: 10.1016/j.engfracmech.2019.05.010
20. Chaudhuri RA. Eigenfunction expansion solutions for three-dimensional rigid planar inclusion problem. Int. J. Fracture 2003; 121(3): 95-110. Doi: 10.1023/B:FRAC.0000005342.29233.86
21. Xie M, Chaudhuri RA. Three-dimensional stress singularity at a bimaterial interface crack front. Compos. Struct. 1997; 40(2): 137-147. Doi:10.1016/S0263-8223(97)00154-2
22. Yoon J, Chaudhuri RA. Three-dimensional asymptotic antiplanet shear stress fields at the front of interfacial crack/anticrack type discontinuities in trimaterial bonded plates. Compos. Struct. 2011; 93 (6): 1505-1515. Doi: 10.1016/j.compstruct.2010.10.016
23. Chaudhuri RA, Yoon, J. Three-dimensional asymptotic mode I/II stress fields at the front of interfacial crack/anticrack discontinuities in trimaterial bonded plates. Compos. Struct. 2012; 94 (2): 351-362. Doi: 10.1016/j.compstruct.2011.07.017
24. Chaudhuri RA, Xie M. On three-dimensional asymptotic solution, and applicability of Saint–Venant's principle to pie-shaped wedge and end face (of a semi-infinite plate) boundary value problems. Eng. Fracture Mech. 2015; 142, 93-107; see also Corrigendum Eng. Fracture Mech. 2019; 217: 106506. Doi: 10.1016/j.engfracmech.2015.04.032
25. Chaudhuri RA. On applicability and uniqueness of the correspondence principle to pie-shaped wedge ("wedge paradox") with various boundary conditions. Eng. Fracture Mech. 2020; 231: 106991. Doi: 10.1016/j.tws.2017.10.013

26. Chaudhuri RA, Xie M. A tale of two saints: St. Venant and "St. Nick" — Does St. Venant's principle apply to bimaterial straight edge and wedge singularity problems?. Compos. Sci. Tech. 2000; 60(12-13): 2503–2515. Doi: 10.1016/S0266-3538(00)00044-0
27. Xie M, Chaudhuri RA. Three-dimensional asymptotic stress field at the front of a bimaterial wedge of symmetric geometry under antiplane shear loading. Compos. Struct. 2001; 54(4): 509-514. Doi: 10.1016/S0263-8223(01)00123-4
28. Chiu JSH, Chaudhuri RA. Three-dimensional asymptotic stress field at the front of an unsymmetric bimaterial pie-shaped wedge under antiplane shear loading. Compos. Struct. 2002; 58(1): 129-137. Doi: 10.1016/S0263-8223(02)00030-2
29. Chaudhuri RA, Xie M. Free-edge stress singularity in a bimaterial laminate. Compos. Struct. 1997; 40(2): 129-136. Doi: 10.1016/S0263-8223(97)00152-9
30. Chaudhuri RA, Chiu SHJ. Three-Dimensional Asymptotic Stress Field in the Vicinity of an Adhesively Bonded Scarf Joint Interface. Compos. Struct. 2009; 89(3): 475-483. Doi: 10.1016/j.compstruct.2008.10.002
31. Chiu SHJ, Chaudhuri RA. A three-dimensional eigenfunction expansion approach for singular stress field near an adhesively-bonded scarf joint interface in a rigidly-encased plate. Eng. Fracture Mech. 2011; 78 (10): 2220-2234. Doi: 10.1016/j.engfracmech.2011.04.009
32. Yoon J, Chaudhuri RA. Three-dimensional asymptotic stress fields at the front of a trimaterial junction. Compos. Struct. 2012; 94 (2): 337-350. Doi: 10.1016/j.compstruct.2011.06.026
33. Chaudhuri RA, Chiu SHJ. Three-dimensional singular stress field near the interfacial bond line of a tapered jointed plate either free-standing (notch) or (fully/partially) attached to a super-rigid inclusion (antinotch). Eng. Fracture Mech. 2012; 91: 87-102. Doi: 10.1016/j.engfracmech.2012.04.011
34. Chaudhuri RA. Three-dimensional asymptotic stress field in the vicinity of the circumferential tip of a fiber-matrix interfacial debond. Int. J. Eng. Sci. 2004; 42(15-16): 1707-1727. Doi: 10.1016/j.ijengsci.2003.12.007
35. Chaudhuri RA. Three-dimensional singular stress field near a partially debonded cylindrical rigid fiber. Compos. Struct. 2006; 72(2): 141-150. Doi: 10.1016/j.compstruct.2004.11.017
36. Chaudhuri SN, Chaudhuri RA, Benner RE, Penugonda M. Raman spectroscopy for characterization of interfacial debonds between carbon fibers and polymer matrices. Compos. Struct. 2006; 76(4): 375-387. Doi: 10.1016/j.compstruct.2005.05.009
37. Chaudhuri RA, Chiu SHJ. Three-dimensional asymptotic stress field at the front of an unsymmetric bimaterial wedge associated with matrix cracking or fiber break. Compos. Struct. 2007; 78(2): 254-263. Doi: 10.1016/j.compstruct.2005.09.013
38. Chaudhuri RA. Three-dimensional asymptotic stress field in the vicinity of the circumference of a penny shaped discontinuity. Int. J. Solids Struct. 2003; 40(13-14): 3787-3805. Doi: 10.1016/S0020-7683(03)00017-9
39. Kaczynski, A. and Kozlowski, W. Thermal stresses in an elastic space with a perfectly rigid flat inclusion under perpendicular heat flow. Int. J. Solids Struct. 2009; 46: 1772-1777. Doi: 10.1016/j.ijsolstr.2009.01.002
40. Willis JR. The penny shaped crack on an interface. Quart. J. Mech. Appl. Math. 1972; 25: 367-385. Doi: 10.1093/qjmam/25.3.367
41. Chaudhuri RA. Three-dimensional asymptotic stress field in the vicinity of the circumference of a bimaterial penny shaped interface discontinuity. Int. J. Fracture 2006; 141(1-2): 207-221. Doi: 10.1007/s10704-006-0076-5
42. Folias ES. The 3D stress field at the intersection of a hole and a free surface. Int. J. Fracture 1987; 35: 187–194.
43. Chaudhuri RA. Three-dimensional asymptotic stress field in the vicinity of the line of intersection of a circular cylindrical through/part-through open/rigidly plugged hole and a plate. Int. J. Fracture 2003; 122(1): 65-88. Doi: 10.1023/B:FRAC.0000005375.68272.c5
44. Folias ES. On interlaminar stresses of a composite plate around the neighborhood of a hole. Int. J. Solids Struct. 1989; 25(10): 1193-1200. Doi: 10.1016/0020-7683(89)90076-0
45. Chaudhuri RA. An eigenfunction expansion solution for three-dimensional stress field in the vicinity of the circumferential line of intersection of a bimaterial interface and a hole. Int. J. Fracture 2004; 129(4): 361-384. Doi: 10.1023/B:FRAC.0000049494.43743.45
46. Folias ES. On the stress singularities at the intersection of a cylindrical inclusion with the free surface of a plate. Int. J. Fracture 1989; 39: 25-34. Doi: 10.1007/BF00047437
47. Chaudhuri RA. Three-dimensional asymptotic stress field in the vicinity of the line of intersection of an inclusion and plate surface. Int. J. Fracture 2002; 117(3): 207-233. Doi: 10.1023/A:1022093101559
48. Chaudhuri RA. Three-dimensional singular stress field at the front of a crack weakening a unidirectional fiber reinforced composite plate. Compos. Struct. 2011; 93(2): 513-527. Doi: 10.1016/j.compstruct.2010.08.028
49. Chaudhuri RA. Three-dimensional singular stress field at the front of a crack and lattice crack deviation (LCD) in a cubic single crystal plate. Philosophical Magazine 2010; 90(15), 2049-2113. Doi: 10.1080/14786430903571412

50. Chaudhuri RA. On three-dimensional singular stress field at the front of a planar rigid inclusion (anticrack) in an orthorhombic mono-crystalline plate. Int. J. Fracture 2012; 174(2): 103-126. Doi: 10.1007/s10704-012-9679-1
51. Chaudhuri RA. Three-dimensional mixed mode I+II+III singular stress field at the front of a (111)[$\bar{1}\,\bar{1}$2]×[1$\bar{1}$0] crack weakening a diamond cubic mono-crystalline plate with crack turning and step/ridge formation. Int. J. Fracture 2014; 187(1): 15-49. Doi: 10.1007/s10704-013-9891-7
52. Chaudhuri RA. On three-dimensional singular stress/residual stress fields at the front of a crack/anticrack in an orthotropic/orthorhombic plate under anti-plane shear loading. Compos. Struct. 2010; 92(8): 1977-1984. Doi: 10.1016/j.compstruct.2009.10.040 (also, Erratum, Compos. Struct. 2011; 93(2): 1058. Doi: 10.1016/j.compstruct.2010.09.010).
53. Chaudhuri RA. Three-dimensional stress/residual stress fields at crack/anticrack fronts in monoclinic plates under antiplane shear loading. Eng. Fracture Mech. 2012; 87: 16-35. Doi: 10.1016/j.engfracmech.2011.12.003
54. Yoon J, Chaudhuri RA. Three-dimensional singular antiplane shear stress fields at the fronts of interfacial crack/anticrack/contact type discontinuities in tricrystal anisotropic plates. Eng. Fracture Mech. 2013; 102: 15–31. Doi: 10.1016/j.engfracmech.2013.01.015
55. Chaudhuri RA. Comparison of stress singularities of kinked carbon and glass fibers weakening compressed unidirectional composites: a three-dimensional trimaterial junction stress singularity analysis. Phil. Magazine 2014; 94(7): 625-667. Doi: 10.1080/14786435.2013.840749
56. Eshelby JD, Read WT, Shockley W. Anisotropic elasticity with application to dislocation theory. Acta Metall. 1953; 1: 251-259. Doi: 10.1016/0001-6160(53)90099-6
57. Carslaw HS. Introduction to the Theory of Fourier Series and Integrals. 3rd edn., Dover, New York (1930).
58. Wilcox CH. Uniqueness theorems for displacement fields with locally finite energy in linear elastostatics. J. Elasticity 1979; 9: 221–243.
59. Chaudhuri RA. Employment of fracture mechanics criteria for accurate assessment of the full set of elastic constants of orthorhombic/tetragonal mono-crystalline YBCO," Applied Mechanics 2023; *4*(2): 585-643. https://doi.org/10.3390/applmech4020032.
60. Riddle J, Gumbsch P, Fischmeister HF. Cleavage Anisotropy in Tungsten Single Crystals. Phys. Rev. Lett. 1996; 76(19): 3594-3597. Doi: 10.1103/PhysRevLett.76.3594
61. Hull D, Beardmore P. Velocity of propagation of cleavage cracks in tungsten. Int. J. Fract. Mech. 1966; 2: 468-487.
62. Perez R, Gumbsch P. Directional anisotropy in the cleavage fracture of silicon. Phys. Rev. Lett. 2000; 84: 5347-5350. Doi: 10.1103/PhysRevLett.84.5347
63. Kermode JR, Albaret T, Sherman D, Bernstein N, Gumbsch P, Payne MC, Csányi G, De Vita A. Low-speed fracture instabilities in a brittle crystal. Nature 2008; 455: 1224-1227. Doi: 10.1038/nature07297
64. Newnham RE. Structure-Property Relations. Springer-Verlag, New York (1975).
65. Pauling L. The Chemical Bond. Cornell Univ. Press, Ithaca, New York (1967).
66. Cotton FA, Wilkinson G. Advanced Inorganic Chemistry. 4th edn., John Wiley & Sons, New York (1980).
67. Alexandrov IV, Goncharov AF, Stishov SM. State equation and compressibility of $YBa_2Cu_3O_x$ high temperature superconductor monocrystals under pressure to 20 GPa. Pis'ma Zh. Eksp. Teor. Fiz. 1988; 47(7): 357-360.
68. Golding B, Haemmerle WH, Schneemeyer LF, Waszczak JV. Gigahertz ultrasound in single crystal superconducting $YBa_2Cu_3O_7$. *IEEE 1988 Ultrasonics Symp. Proc.* Chicago, IL, 1988; vol.2: 1079-1083. Doi: 10.1109/ULTSYM.1988.49544
69. Saint-Paul M, Tholence JL, Noel H, Levet JC, Potel M, Gougeon P. Ultrasound study on $YBa_2Cu_3O_{7-\delta}$ and $GdBa_2Cu_3O_{7-\delta}$ single crystals. Solid State Comm. 1989; 69(12): 1161-1163. Doi: 10.1016/0038-1098(89)91055-7
70. Saint-Paul M, Henry JY. Elastic anomalies in $YBa_2Cu_3O_{7-\delta}$ single crystals. Solid State Communications 1989; 72(7): 685-687. Doi: 10.1016/0038-1098(89)90674-1
71. Jorgensen, JD, Pei S, Lightfoot P, Hinks DG, Veal BW, Dabrowski B, Paulikas AP, Kleb R, Brown ID. Physica C 1990; 171, 93-
72. Reichardt W, Pintschovius L, Hennion B, Collin F. Inelastic neutron scattering study of $YBa_2Cu_3O_{7-x}$. Supercond. Sci. Tech. 1988; 1(4): 173-176. Doi: 10.1088/0953-2048/1/4/004
73. Baumgart P, Blumenröder S, Erle A, Hillebrands B, Güntherodt G, Schmidt H. Sound velocities of $YBa_2Cu_3O_{7-\delta}$ single crystals measured by Brillouin spectroscopy. Solid State Comm. 1989; 69(12): 1135-1137. Doi: 10.1016/0038-1098(89)91049-1
74. Baumgart P, Blumenröder S, Erle A, Hillebrands B, Splittgerber P, Güntherodt G, Schmidt H. Sound velocities of $YBa_2Cu_3O_{7-\delta}$ and $Bi_2Sr_2CaCu_2O_x$ single crystals measured by Brillouin spectroscopy. Physica C: Supercond. Its Applic. 1989; 162–164, Part 2: 1073-1074. Doi: 10.1016/0921-4534(89)90599-6

75. Zouboulis E, Kumar S, Chen CH, Chan SK, Grimsditch M, Downey J, McNeil L, Surface waves on the a, b and c faces of untwinned single crystals of $YBa_2C_3O_{7-\delta}$. Physica C: Superconductivity 1992; 190(3): 329-332. Doi: 10.1016/0921-4534(92)90614-I
76. Lei M, Sarrao JL, Visscher WM, Bell TM, Thompson JD, Migliori A, Welp UW, Veal BM. Elastic constants of a monocrystal of superconducting $YBa_2Cu_3O_{7-\delta}$. Phys. Rev. B 1993; 10: 6154-6156. Doi: 10.1103/PhysRevB.47.6154
77. Migliori A, et al. Elastic constants and specific-heat measurements on single crystals of La2CuO4. Phys. Rev. B 1990; 41: 2098-2102. Doi: 10.1103/PhysRevB.41.2098
78. Nye JF. Physical Properties of Crystals. Oxford University Press, Oxford (1979).
79. D. J. Weidner and G. Simmons. J. Geophys. Res. 77 (1972) 826-847.
80. Cook RF, Dinger TR, Clarke DR. Fracture toughness measurements of YBa2Cu3Ox single crystals. Appl. Phys. Lett. 1987; 61: 454-456. Doi: 10.1063/1.98420
81. Raynes AS, Freiman SW, Gayle FW, Kaiser DL. Fracture toughness of $YBa_2Cu_3O_{6+\delta}$ single crystals: Anisotropy and twinning effects. J. Appl. Phys. 1991; 70 (10), 5254-5257. Doi: 10.1063/1.350234
82. Goyal A, Funkenbusch PD, Kroeger DM, Burns SJ. Anisotropic hardness and fracture toughness of highly aligned $YBa_2Cu_3O_{7-\delta}$. J. Appl. Phys. 1992; 71(5): 2363-2366. Doi: 10.1063/1.351090
83. Granozio FM, di Uccio US. Gibbs energy and growth habits of YBCO. J. Alloys and Compounds 1997; 251(1-2): 56-64. Doi: 10.1016/S0925-8388(96)02769-7
84. Streiffer SK, Lairson BM., Eom CB, Clemens BM, Bravman JC, Geballe TH. Microstructure of ultrathin films of $YBa_2Cu_3O_{7-\delta}$ on MgO. Phys. Rev. B 1991; 43: 13007. Doi: 10.1103/PhysRevB.43.13007
85. Fowler DE, Brundle C.R., Lerczac J, Holtzberg FJ. Core and valence XPS spectra of clean, cleaved single crystals of $YBa_2Cu_3O_7$. Electron Spectroscopy and Related Phenomena 1990; 52: 323-339. Doi: 10.1016/0368-2048(90)85029-9
86. Tanaka S, Nakamura T, Tokuda H, Iiyama M. All *in situ* deposition and characterization of $YBa_2Cu_3O_{7-x}$ thin films by low-energy electron diffraction and low-energy ion scattering spectroscopy. Appl. Phys. Lett. 1993; 62: 3040. Doi: 10.1063/1.109132
87. Lin CT, Liang WY. Etch defects in $YBa_2Cu_3O_{7-\delta}$ single crystals grown from flux. Physic C 1994; 225: 275-286. Doi: 10.1016/0921-4534(94)90724-2
88. Chaudhuri RA. Interfacial Crack Turning in Bi-Crystals of Cubic Symmetry: A Three-Dimensional Stress Singularity Analysis. In Fracture Mechanics: Advances in Research and Applications, ed., R. D. S. G. Campilho, K. Madani, and M. Belhouari, Nova Science Publishers, Inc., 2024.
89. Chaudhuri RA, El-Gerwi LA. Estimation of residual stresses in a pressurized thin cylindrical vessel weakened by a finite line crack. *In Fracture Mechanics: Advances in Research and Applications,* ed., R. D. S. G. Campilho, K. Madani, and M. Belhouari, Nova Science Publishers, Inc., 2024.
90. Comninou, M. The interface crack. ASME J. Appl. Mech. 1977; 44: 631-636.
91. Hull D, Clyne TW. An Introduction to Composite Materials. 2nd edn., Cambridge, UK; Cambridge University Press, 1996.
92. Tuinstra F, Koenig JL. Characterization of graphite fiber surfaces with Raman spectroscopy. Journal of Composite Materials 1970; 4: 492-499.